

1 **Understanding the spatio-temporal variability of tropical orographic rainfall  
2 using convective plume buoyancy**

3 Quentin Nicolas<sup>a</sup> and William R. Boos<sup>a,b</sup>

4 <sup>a</sup>*Department of Earth and Planetary Science, University of California, Berkeley, California*

5 <sup>b</sup>*Climate and Ecosystem Sciences Division, Lawrence Berkeley National Laboratory, Berkeley,  
6 California*

7 *Corresponding author:* Quentin Nicolas, qnicolas@berkeley.edu

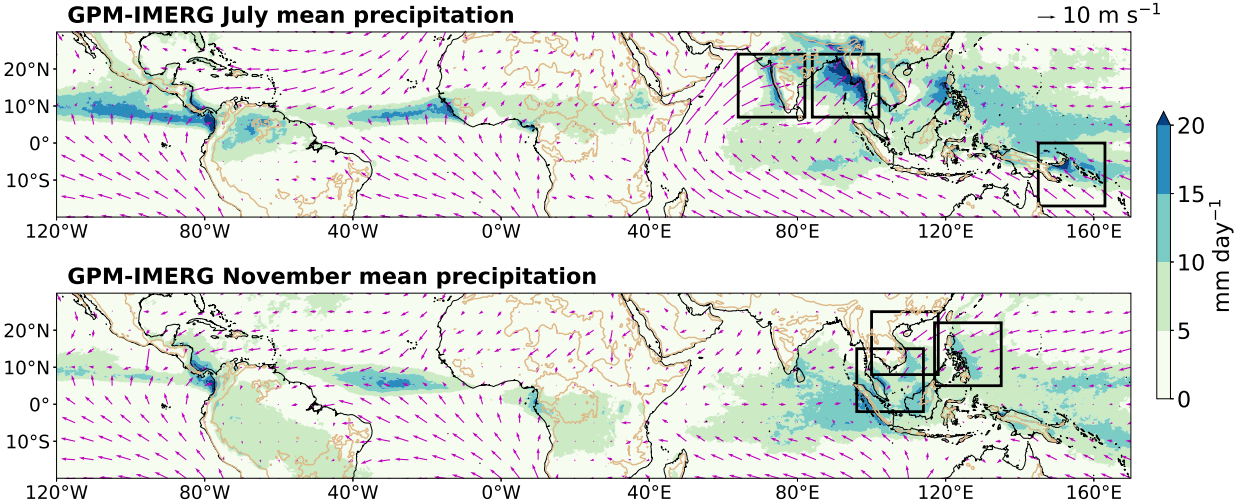
8 ABSTRACT: Mechanical forcing by orography affects precipitating convection across many trop-  
9 ical regions, but controls on the intensity and horizontal extent of the orographic precipitation  
10 peak and rain shadow remain poorly understood. A recent theory explains this control of precip-  
11 itation as arising from modulation of lower-tropospheric temperature and moisture by orographic  
12 mechanical forcing, setting the distribution of convective rainfall by controlling parcel buoyancy.  
13 Using satellite and reanalysis data, we evaluate this theory by investigating spatio-temporal precip-  
14 itation variations in six mountainous tropical regions spanning South and Southeast Asia, and the  
15 Maritime Continent. We show that a strong relationship holds in these regions between daily pre-  
16 cipitation and a measure of convective plume buoyancy. This measure depends on boundary layer  
17 thermodynamic properties and lower-free-tropospheric moisture and temperature. Consistent with  
18 the theory, temporal variations in lower-free-tropospheric temperature are primarily modulated by  
19 orographic mechanical lifting through changes in cross-slope wind speed. However, winds di-  
20 rected along background horizontal moisture gradients also influence lower-tropospheric moisture  
21 variations in some regions. The buoyancy measure is also shown to explain many aspects of the  
22 spatial patterns of precipitation. Finally, we present a linear model with two horizontal dimen-  
23 sions that combines mountain wave dynamics with a linearized closure exploiting the relationship  
24 between precipitation and plume buoyancy. In some regions, this model skillfully captures the  
25 spatial structure and intensity of rainfall; it underestimates rainfall in regions where time-mean  
26 ascent in large-scale convergence zones shapes lower-tropospheric humidity. Overall, these results  
27 provide new understanding of fundamental processes controlling subseasonal and spatial variations  
28 in tropical orographic precipitation.

29 **1. Introduction**

30 Mountains shape rainfall distributions in many of Earth's tropical land regions, modifying the  
31 thermodynamic environment by interacting with large-scale winds or altering surface fluxes. With  
32 over 2.5 billion people living in mountainous areas and another 2 billion in lowland areas depending  
33 on mountain water resources (Viviroli et al. 2020), orographic precipitation is currently the main  
34 water source for over 55% of the world's population, mostly in the tropics. It is also the main  
35 source of energy for hydropower, which is the primary resource for renewable electricity generation  
36 globally, and a potential cause of dam failures when occurring in excess (Li et al. 2022).

37 Orographic rainfall features large spatial gradients, with vastly different hydrological conditions  
38 upwind and downwind of ridges. The qualitative picture is widely known: mountains force  
39 low-level ascent on their upwind flanks, which, with sufficient moisture, drives condensation and  
40 precipitation (Smith 1979; Roe 2005). The subsiding downstream flow, conversely, is warm and  
41 dry. In the tropics, strong precipitation gradients are widely observed along local orography in  
42 South and Southeast Asia, the Maritime Continent, and the northern and central Andes (Fig. 1).  
43 The spatial structure of orographic precipitation has been studied in various regions across the  
44 tropics, with examples including the Ethiopian Highlands (Van den Hende et al. 2021), the Andes  
45 (Espinoza et al. 2015), the Western Ghats (e.g. Tawde and Singh 2015) and the Arakan Yoma  
46 range of Myanmar (e.g. Shige et al. 2017). Yet the above paradigm, which assumes layer-wise  
47 ascent and saturation, is unlikely to be quantitatively accurate in these regions where most rainfall  
48 stems from convection (Kirshbaum et al. 2018) and where even simple questions such as what sets  
49 the upstream extent of orographic rainfall enhancement have been debated (Smith and Lin 1983;  
50 Grossman and Durran 1984). This study aims to address this issue and related open questions (such  
51 as controls on rain shadow extent and the amplitude of rainfall maxima), taking several tropical  
52 regions as examples.

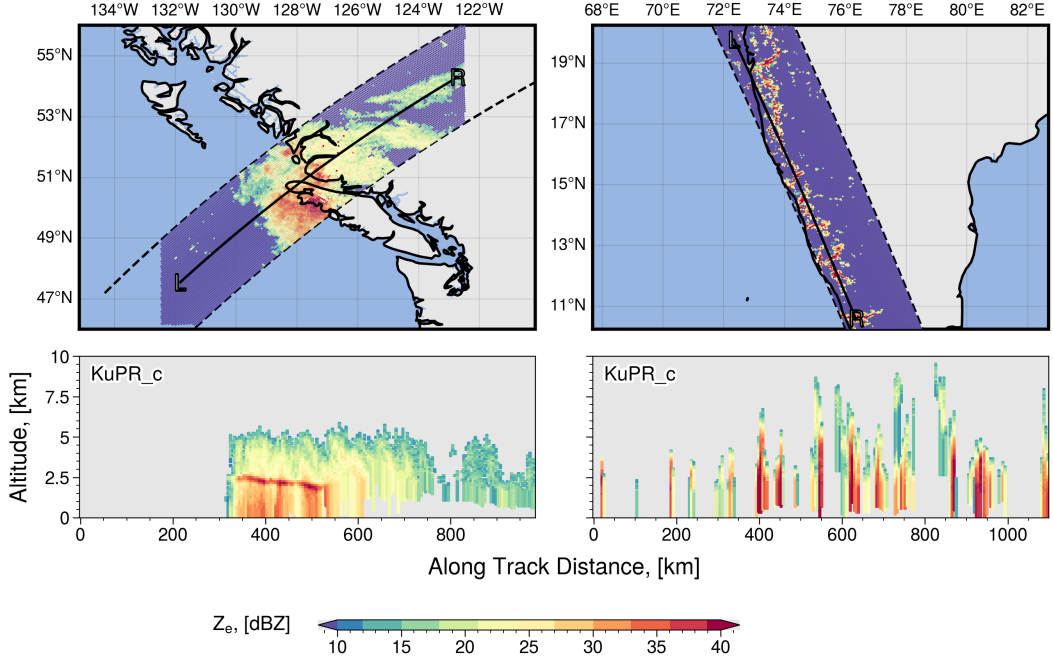
56 In midlatitudes, column-integrated water vapor transport (IVT) has been proposed as a dom-  
57 inant control on orographic precipitation (Sawyer 1956; Smith 2018). Indeed, in the idealized  
58 picture of forced ascent over an orographic barrier, IVT modulates the condensation rate over the  
59 upwind slopes. Additionally, stronger IVT typically results in a smaller nondimensional mountain  
60 height (through both stronger winds and a smaller effective static stability), causing flow to ascend  
61 rather than detour around mountains (Smith 1989; Kirshbaum and Smith 2008). Other controls



53     FIG. 1. IMERG V06B precipitation (Huffman et al. 2019, shading), 500 m surface height level (thin brown  
 54     contours), and ERA5 wind vectors 100 m above the surface (Hersbach et al. 2018) averaged over June (top) and  
 55     November (bottom) from 2001 to 2020.

62     on midlatitude orographic precipitation include mountain slope and temperature-mediated micro-  
 63     physical effects (Kirshbaum and Smith 2008). The spatial organization of orographic precipitation  
 64     in convectively stable flows has been understood through the influence of topography on vertical  
 65     velocities in saturated flows, with a contribution from the downwind advection of hydrometeors  
 66     (Smith and Barstad 2004, hereafter SB04).

67     Orographic precipitation generally occurs in association with various types of disturbances, from  
 68     frontal systems in midlatitude winter to deep convective systems in parts of the tropics (Houze  
 69     2012). We illustrate these in Fig. 2, which shows instantaneous radar reflectivity from the Global  
 70     Precipitation Measurement (GPM) Ku-band radar (Iguchi and Meneghini 2021) for two cases. The  
 71     first illustrates a winter frontal system over coastal mountains of British Columbia and features a  
 72     wide, shallow signal with a sloping bright band (visible between 300 and 550 km at 2 km altitude  
 73     in the vertical cross-section), characteristic of frontal ascent. In contrast, the Western Ghats case,  
 74     during the summer monsoon, features smaller scale, stronger echoes reaching deeper heights (6-10  
 75     km; note that summertime convection in and upstream of the Western Ghats is shallower than in  
 76     the rest of the tropics, see Kumar and Bhat 2017). While wide radar echoes are also observed in the



79 FIG. 2. Near-surface radar reflectivity from the Ku-band GPM radar (top) and vertical cross-section of corrected  
 80 Ku-band reflectivity (bottom) for two overpasses : July 20<sup>th</sup>, 2014 over the Western Ghats (left) and February 11<sup>th</sup>,  
 81 2015 over the coast range of British Columbia (right). The black lines on the top panels show the location of the  
 82 cross-sections on the bottom panels, with the L and R marks corresponding to the left/right of the cross-sections.

77 tropics, such as in mesoscale convective systems (Houze et al. 2015), such systems reach deeper  
 78 heights than winter midlatitude storms.

83 Tropical orographic precipitation is more even in time than surrounding land or oceanic pre-  
 84 cipitation (Van den Hende et al. 2021; Espinoza et al. 2015; Sobel et al. 2011). Nevertheless,  
 85 intraseasonal and interannual variability in orographic rainfall seems to be influenced by the  
 86 classical tropical modes that regulate moist convection. Examples include the boreal summer in-  
 87 traseasonal oscillation (BSISO, Shige et al. 2017; Hunt et al. 2021), the Madden-Julian Oscillation  
 88 (MJO, Bagtasa 2020) and large-scale interannual modes such as the El Niño-Southern Oscillation  
 89 and the Indian Ocean Dipole (Yen et al. 2011; Revadekar et al. 2018; Lyon et al. 2006; Smith et al.  
 90 2013). Hence, it appears that any successful theory for tropical orographic precipitation needs to  
 91 address the question of how mountains interact with moist convection.

92 Boundary-layer moist static energy and free-tropospheric temperature regulate moist convection  
 93 by influencing column stability. Observations and simulations have shown that free-tropospheric

water vapor also exerts a strong control on precipitation, consistent with the idea that entrainment of free-tropospheric air modulates plume buoyancy (e.g. Derbyshire et al. 2004). Tropical rainfall thus appears to be jointly influenced by free-tropospheric temperature and moisture, and interacts with slower, balanced dynamics to eliminate positive perturbations in these quantities—a behavior termed lower-tropospheric quasi-equilibrium (QE, e.g. Raymond et al. 2015). The prominent role of lower-tropospheric moisture has been confirmed in observations of orographic convection at low latitudes (Hunt et al. 2021; Connor Nelson et al. 2022). Beyond the lower-tropospheric thermodynamic environment, factors such as the wind profile—especially vertical wind shear, which one could expect to be important in the presence of mountain waves—should affect deep convective development (Robe and Emanuel 2001; Anber et al. 2014, see e.g.). We do not consider such factors here.

Ahmed et al. (2020) cast the observed dependence of tropical convection on the lower-tropospheric thermodynamic environment into a simple buoyancy-based framework. Precipitation is strongly controlled by a measure of plume buoyancy that takes into account the influences of instability and entrainment, and depends on boundary layer equivalent potential temperature as well as lower-free-tropospheric temperature and moisture. We recently posited (Nicolas and Boos 2022, hereafter NB22) that mechanically forced orographic convection can be understood in this framework, with stationary mountain waves disturbing lower-free-tropospheric thermodynamics, in turn affecting precipitation. We developed a linear model for the spatial distribution of rainfall, combining orographic gravity wave dynamics with the linearized QE closure of Ahmed et al. (2020). That model assumes a simple background state that has horizontally uniform temperature and moisture profiles, with horizontally and vertically uniform wind. At first order, the temperature and moisture perturbations are dictated by vertical displacement in a mountain wave, which is in turn controlled by the topographic shape, cross-slope wind, and static stability. The normalized gross moist stability (e.g. Raymond et al. 2009) appears as a second-order control, because it modulates convective moisture relaxation. One goal of the present work is to evaluate to what extent this framework can explain observed spatial patterns of orographic tropical rainfall. The present work extends this framework to two horizontal dimensions and assesses whether it explains observed spatial patterns of orographic tropical rainfall.

More generally, this study explores the physical drivers behind the temporal variations and spatial structure of orographic precipitation around six tropical mountain regions: the Western Ghats (India), the western coast of Myanmar (Arakan Yoma mountain range), the eastern coast of Vietnam (Annamite mountains), the Malay peninsula, the Philippines, and the island of New Britain (Papua New Guinea). We justify the use of a lower-tropospheric buoyancy measure in quantifying daily orographic precipitation variability and explore the dominant controls on its components—both within the boundary layer and the lower-free-troposphere. We then explore to what extent time-averages of this buoyancy measure account for observed spatial patterns of rainfall, and test the QE-based linear theory of NB22 against observations.

## 2. Data

We use the IMERG V06B precipitation dataset (Huffman et al. 2019), which combines satellite-based infrared and passive microwave measurements with rain gauge data to provide hourly estimates at  $0.1^\circ$  resolution. IMERG is known to suffer from biases in regions of complex topography relative to rain gauge measurements. These biases are reduced when considering spatial or temporal averages (Pradhan et al. 2022). In section 4, we use daily precipitation averages at large spatial scales, and the regions over which we are averaging contain between 45% and 80% of ocean points, over which confidence in IMERG retrievals is higher. In sections 3 and 6, we consider seasonal averages, which are calibrated using gauge data and have accordingly little bias (Derin et al. 2019).

We evaluate the thermodynamic environment and horizontal winds from the ERA5 reanalysis (Hersbach et al. 2018), which provides hourly data at  $0.25^\circ$  resolution. Johnston et al. (2021) showed that moisture soundings from ERA5 had excellent agreement with satellite-based radio occultation retrievals in the tropics and subtropics. Proper evaluation of ERA5 lower-tropospheric temperature is lacking; we note that Hersbach et al. (2020) showed improved 850 hPa temperature estimates (when compared to radiosondes) over ERA-Interim, especially in the past two decades.

Unless otherwise specified, we use topography from the ETOPO1 global relief model (National Geophysical Data Center 2011; Amante and Eakins 2008), at 60 arc-second resolution.

<sup>149</sup> **3. Selecting regions of mechanically forced tropical orographic rainfall**

<sup>150</sup> To illustrate the physical drivers of tropical orographic precipitation, we select six regions in  
<sup>151</sup> South Asia and the Maritime Continent. We focus on mechanically forced convection, a regime  
<sup>152</sup> in which orographic forcing is felt through the forced uplift of impinging flow, by opposition to  
<sup>153</sup> thermal forcing, where the diurnal cycle of heating over sloped terrain drives low-level convergence.  
<sup>154</sup> The wind speed threshold marking the transition from thermal to mechanical forcing depends  
<sup>155</sup> on various factors including stability  $N$  and mountain height  $h_m$ . One quantity often used to  
<sup>156</sup> characterize orographic flows is the nondimensional mountain height,  $M = Nh_m/U$ , where  $U$  is  
<sup>157</sup> the cross-slope wind speed. Flows with  $M < 1$  tend to cross topography (rather than being blocked  
<sup>158</sup> upstream), which may prevent the development of thermally-forced circulations (Kirshbaum et al.  
<sup>159</sup> 2018). For moderately high mountains (500-1000 m) in the tropics, various studies have suggested  
<sup>160</sup> that mechanical forcing dominates above about  $5 \text{ m s}^{-1}$  (Nugent et al. 2014; Wang and Sobel 2017).  
<sup>161</sup> Accordingly, we selected regions with a mean upstream wind higher than  $6 \text{ m s}^{-1}$  and a visible  
<sup>162</sup> orographic rain band. These regions are outlined in Fig. 1, with close-up views of their topography  
<sup>163</sup> and seasonal-mean rainfall and wind in Fig. 3.

<sup>164</sup> Three of these regions have their雨iest season in boreal summer (June-August). The Western  
<sup>165</sup> Ghats, a mountain range located on the west coast of peninsular India, form a kilometer-high barrier  
<sup>166</sup> to the southwesterly monsoon flow. With  $M \approx 0.8$  (measuring wind speed 500 km upstream of the  
<sup>167</sup> coast and 100 m above the surface), the Ghats fall within a clear mechanically forced regime, as  
<sup>168</sup> attested by the small diurnal cycle of rainfall there (Shige et al. 2017). The dynamics of orographic  
<sup>169</sup> precipitation in the Western Ghats have been the subject of several modeling studies (Smith and  
<sup>170</sup> Lin 1983; Grossman and Durran 1984; Ogura and Yoshizaki 1988; Xie et al. 2006; Oouchi et al.  
<sup>171</sup> 2009; Sijikumar et al. 2013; Zhang and Smith 2018). These studies confirm that the presence  
<sup>172</sup> of orography is crucial in producing the observed rain band, and (expectedly) that latent heating  
<sup>173</sup> cannot be neglected in describing the orographic flow.

<sup>174</sup> The Arakan Yoma mountain range, located along the coast of Myanmar, also interacts with the  
<sup>175</sup> Asian summer monsoon (Xie et al. 2006; Oouchi et al. 2009; Wu et al. 2018). With maximum  
<sup>176</sup> seasonal-mean precipitation values exceeding  $30 \text{ mm day}^{-1}$  upstream of the range, it is responsible  
<sup>177</sup> for the strongest rain band on Earth in boreal summer. Compared to the Western Ghats, convection

178 is deeper and of wider scale upstream of Myanmar, a fact that Shrestha et al. (2015) associated  
179 with differences in lower tropospheric humidity.  $M$  has a similar value around 0.8 there.

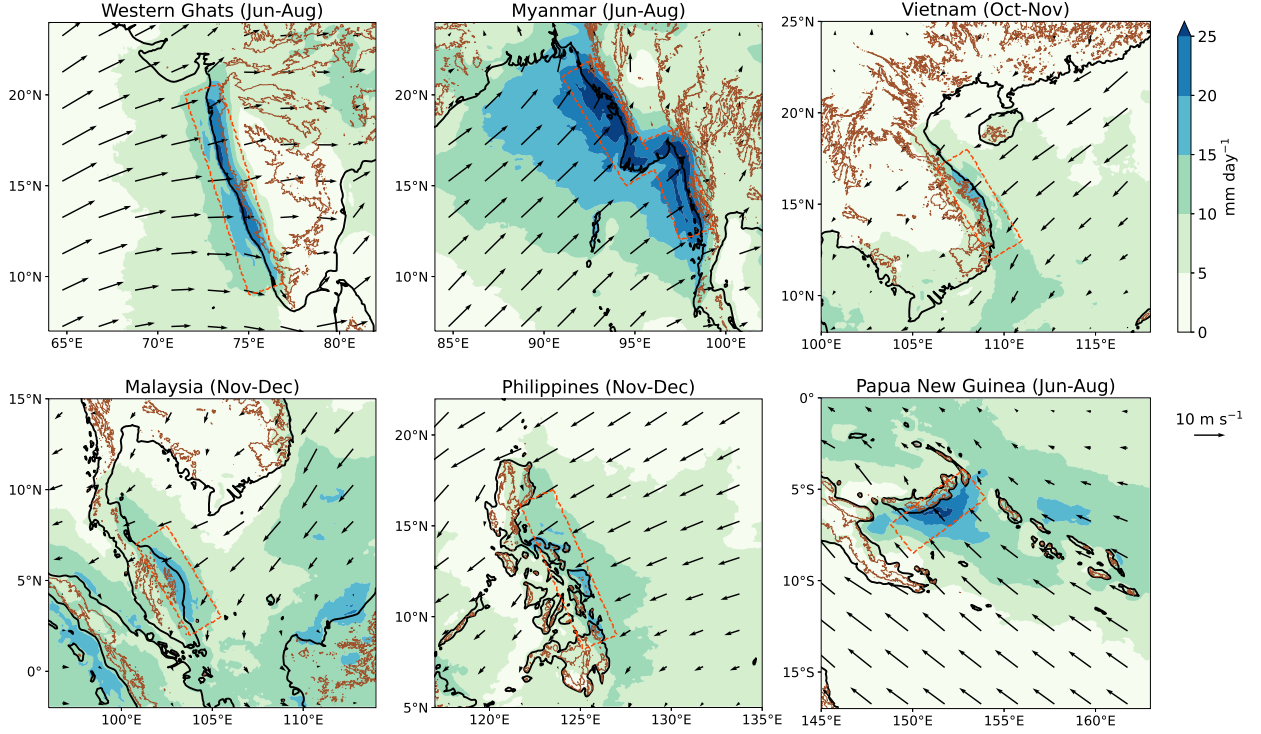
180 The island of New Britain, in Papua New Guinea (hereafter PNG), is our third region of interest  
181 in boreal summer. The mountains are of modest height there (300 m when averaging across the  
182 island, although individual peaks exceed 2 km), but a strong precipitation band reaching 25 mm  
183 day $^{-1}$  lies upstream of the island. Winds speeds around 8-9 m s $^{-1}$  yield a nondimensional mountain  
184 height  $M \approx 0.4$ . Orographic rainfall in PNG has been the focus of a few studies (e.g. Biasutti et al.  
185 2012; Smith et al. 2013).

186 The remaining three regions are associated with boreal autumn rainfall. The coast of Vietnam,  
187 east of the Annamite range, receives most of its rainfall in October and November (Chen et al.  
188 2012; Ramesh et al. 2021), in association with an onshore cross-slope wind of 8-9 m s $^{-1}$  during  
189 this season ( $M = 1$ ). The eastern coast of the Philippines experiences a late autumn precipitation  
190 peak (November-December) with a similar wind speed and  $M = 0.3$  (Chang et al. 2005; Robertson  
191 et al. 2011). These two regions experience a second rainfall peak in boreal summer on the opposite  
192 side of their mountain ranges, associated with reversed winds during the summer monsoon (see  
193 Fig. 1). Because the winds are not as strong then, the dominance of mechanical forcing cannot be  
194 clearly established, and we did not include these secondary rain seasons in our analysis. Finally, the  
195 Eastern half of the Malay Peninsula also receives most of its rainfall in November and December  
196 (Chen et al. 2013), similarly associated with mechanical orographic forcing ( $M = 0.5$ ).

200 To streamline the presentation, the study was limited to six regions. This sample is not an  
201 exhaustive representation of tropical orographic rainfall, although we think it is quite representative  
202 of mechanically forced cases.

#### 203 **4. Controls on daily variations of orographic rainfall**

204 In the tropics, mechanically forced orographic rainfall is subject to less temporal variability than  
205 rainfall over surrounding land and ocean. In particular, it has a weak diurnal cycle, as noted by  
206 Shige et al. (2017) in the Western Ghats and in Myanmar. This can be understood as resulting  
207 from daytime heating of the boundary layer being limited by the ventilation resulting from strong  
208 wind (e.g. Nugent et al. 2014). The distribution of daily rainfall within regions where mechanical  
209 forcing dominates is also more uniform, with less contribution from extreme days. This was noted



197 FIG. 3. IMERG V06B precipitation, 500 m surface height level (thin magenta contours), and ERA5 wind  
 198 vectors 100 m above the surface in six tropical regions, averaged over each region's雨季 (see text)  
 199 from 2001 to 2020.

213 TABLE 1. Percentage of seasonal rainfall contributed by the rainiest days (defined as days and locations where  
 214 rainfall is above the 90<sup>th</sup> percentile), in the whole region and within the orographic rain band, for each region  
 215 studied. The rain bands are defined by the red dashed rectangles in Fig. 3.

Region name	Whole region	Orographic rain band
Western Ghats	74	53
Myanmar	59	43
Vietnam	80	73
Malaysia	63	61
Philippines	76	66
PNG	70	55

210 by Espinoza et al. (2015) in the Central Andes and is confirmed for regions studied here (Table 1).  
 211 Nevertheless, these regions still show substantial subseasonal rainfall variations. The goal of this  
 212 section is to determine the factors governing these temporal variations of daily-mean precipitation.

216 *a. Dynamic and thermodynamic predictors of daily rainfall variations*

217 The canonical picture of orographic rainfall highlights the importance of the cross-slope vapor  
218 transport in governing rain rates (Smith 2018). In a saturated atmosphere ascending with velocity  
219  $w$ , the column-integrated condensation rate is

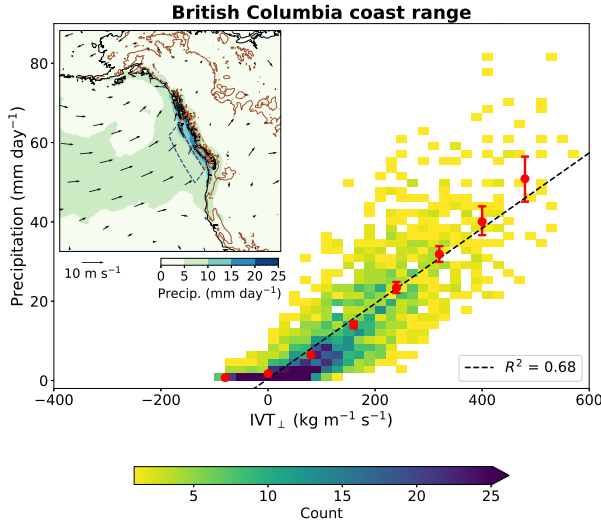
$$C = - \int_0^\infty w \frac{d(\rho q_{\text{sat}})}{dz} dz. \quad (1)$$

220 The water vapor density can be approximated as decreasing exponentially with  $z$ , with a scale height  
221  $H_{\text{sat}}$ . If  $\mathbf{u}$  denotes the surface horizontal wind and  $h$  the surface height, then  $w(z=0) = \mathbf{u} \cdot \nabla h$ . In  
222 the simplest approximation where  $w$  is vertically uniform, then

$$C = \int_0^\infty (\mathbf{u} \cdot \nabla h) \frac{\rho q_{\text{sat}}}{H_{\text{sat}}} dz = \frac{\mathbf{IVT} \cdot \nabla h}{H_{\text{sat}}}, \quad (2)$$

223 where **IVT** denotes the vertically integrated water vapor transport. Setting precipitation equal to  
224 the product of  $C$  with a precipitation efficiency, one sees that in this so-called upslope model, it  
225 is proportional to the cross-slope IVT. This model is widely considered to have many shortcom-  
226 ings, including the assumption of a saturated atmosphere and the oversimplified vertical velocity  
227 parameterization. Nevertheless, it skillfully characterizes temporal rainfall variations in some mid-  
228 latitude mountain ranges, as illustrated for the British Columbia coastal range in Fig. 4: despite  
229 some scatter, daily precipitation rates in winter are decently described by a linear relationship  
230 with cross-slope IVT (hereafter  $\text{IVT}_{\perp}$ ). Although the vertically uniform ascent model for vertical  
231 velocity ( $w = \mathbf{u} \cdot \nabla h$ ) is crude, it captures the simple fact that vertical velocities in convectively  
232 stable orographic flows are mostly controlled by cross-slope wind. Deviations from this simple  
233 picture, including the specific dynamics of various types of weather systems, yield the scatter.

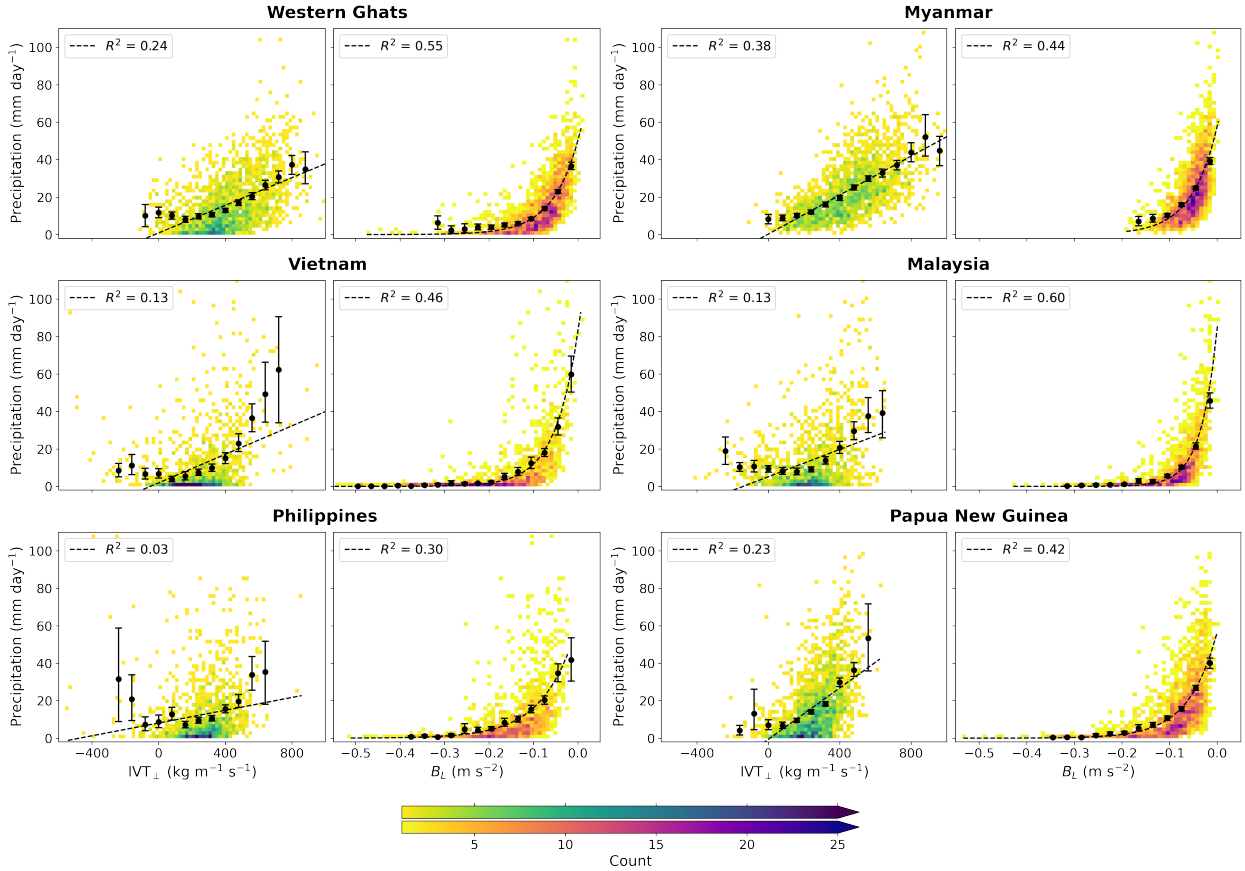
234 In the tropics, where convective ascent is more important, one might expect other factors than  
235 cross-barrier winds to modulate ascent rates. Still, Bagtasa (2020) suggested that enhanced cross-  
236 slope winds in the Philippines associated with certain phases of the MJO favored rainfall in late  
237 autumn. Similarly, Shige et al. (2017) showed that rainfall in the Western Ghats and the Arakan  
238 Yoma range of Myanmar was in phase with the southwesterly wind strength modulated by the  
239 BSISO. This suggests that cross-slope winds, and perhaps cross-slope IVT, still are important  
240 controls on orographic precipitation at low latitudes. Figure 5 (first and third columns) shows the



223 FIG. 4. Joint distributions of daily cross-slope IVT and precipitation in the coast range of British Columbia.  
 224 Precipitation is averaged over the orographic rain band (red box in the inset). Cross-slope IVT (defined as its  
 225 northeastward component) is averaged immediately upstream of the precipitation maximum (blue dashed box  
 226 in the inset). The black dashed line shows the best linear fit. The black dots represent conditionally averaged  
 227 precipitation over bins of width  $80 \text{ kg m}^{-1}\text{s}^{-1}$ , with error bars representing a 95% confidence interval obtained  
 228 by bootstrapping. The inset shows climatological rain and wind averaged over November–January.

256 joint distributions of  $\text{IVT}_\perp$  and precipitation, as well as precipitation conditionally averaged on  
 257  $\text{IVT}_\perp$ . While a positive relationship remains, it does not hold as strongly as in the midlatitude  
 258 winter case shown in Fig. 4, with numerous dry days associated with strong  $\text{IVT}_\perp$ . We thus seek  
 259 another metric to characterize temporal variations in tropical orographic rainfall.

260 The question of what environmental factors set convective precipitation rates is at the heart of  
 261 any theory of tropical atmospheric dynamics. The quasiequilibrium hypothesis (QE, e.g. Emanuel  
 262 et al. 1994) states that convection acts to deplete anomalies in convective available potential energy  
 263 (CAPE). This description predicts the effect moist convection has on its environment, consuming  
 264 instability and setting vertical temperature profiles close to moist adiabats. However, it alone  
 265 does not provide information on convective intensity or precipitation rates, given environmental  
 266 conditions. One further development stems from the observed exponential dependence of precip-  
 267 itation rates on column moisture content (e.g. Bretherton et al. 2004). The physical roots of this  
 268 dependence lie in the effect that entrainment of free-tropospheric air has on plume buoyancy.



240 FIG. 5. Joint distributions of daily cross-slope IVT and precipitation (first and third columns, green colors)  
 241 and  $B_L$  and precipitation (second and fourth columns, red colors).  $B_L$  and precipitation are averaged spatially  
 242 over the rain band regions (red boxes in Fig. 3). IVT is averaged right upstream of the rain band regions,  
 243 in boxes of the same size and orientation. The cross-slope direction is defined as 70° (Ghats), 60° (Myanmar), 240°  
 244 (Vietnam), 225° (Malaysia), 225° (Philippines), and 320° (PNG). Linear fits (for the IVT-precipitation relation)  
 245 and exponential fits (for the  $B_L$ -precipitation relation) are shown as dashed lines, with the associated coefficients  
 246 of determination in the legend. The black dots represent conditionally averaged precipitation over bins of width  
 247 80 kg m<sup>-1</sup> s<sup>-1</sup> (for IVT) and 0.03 m s<sup>-2</sup> (for  $B_L$ ), with error bars representing a 95% confidence interval obtained  
 248 by bootstrapping.

269 Seeking a unified measure that would characterize rainfall across the tropics, Ahmed and Neelin  
 270 (2018) derived an expression for a lower-tropospheric averaged plume buoyancy, that only depends  
 271 on environmental temperature and moisture profiles. Dividing the lower atmosphere in two layers,

<sup>272</sup> a boundary layer (subscript  $B$ ) and a lower-free-troposphere<sup>1</sup> (subscript  $L$ ), this expression reads  
<sup>273</sup> (Ahmed et al. 2020)

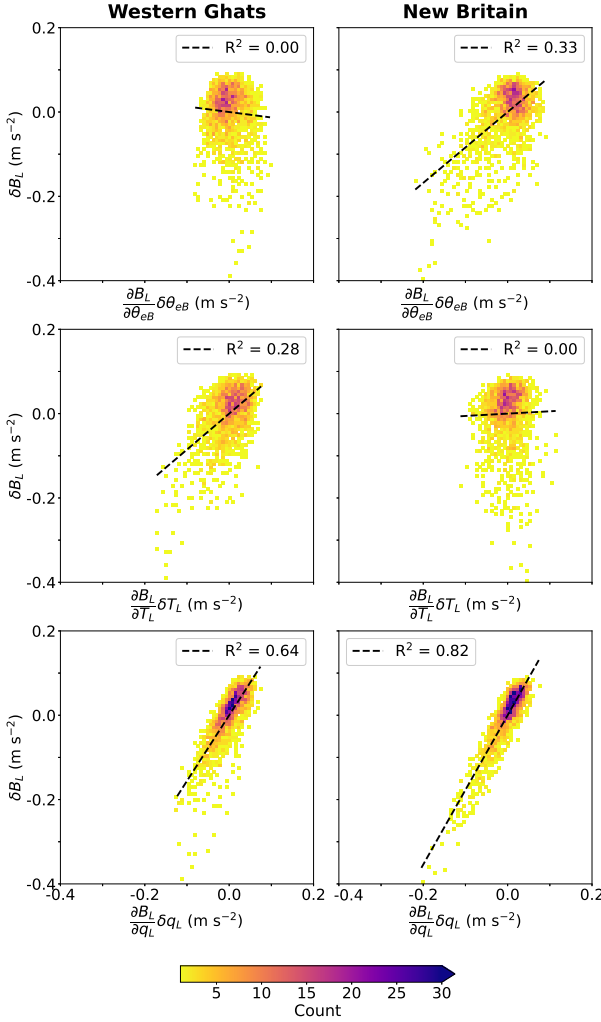
$$B_L = g \left[ \alpha_B \frac{\theta_{eB} - \theta_{eL}^*}{\theta_{eL}^*} - \alpha_L \frac{\theta_{eL}^* - \theta_{eL}}{\theta_{eL}^*} \right], \quad (3)$$

<sup>274</sup> where  $g$  is the acceleration of gravity,  $\theta_e$  is equivalent potential temperature (and  $\theta_e^*$  its saturated  
<sup>275</sup> value), and subscripts denote averages taken over respective layers. The weights  $\alpha_B$  and  $\alpha_L = 1 - \alpha_B$   
<sup>276</sup> depend on the thickness of each layer and the assumed mass flux profile of the plume. We use  
<sup>277</sup>  $\alpha_B = 0.52$  (as in Ahmed et al. 2020). The first term in (3) is a CAPE-like term, wherein the  
<sup>278</sup> difference between boundary layer  $\theta_e$  and lower-free-tropospheric  $\theta_e^*$  provides a measure of moist  
<sup>279</sup> convective instability. The second term describes subsaturation of the lower free troposphere,  
<sup>280</sup> and quantifies the efficiency of entrainment at reducing buoyancy by drying the plume (hence the  
<sup>281</sup> negative sign in front of it).

<sup>290</sup> When conditionally averaged on  $B_L$  (at  $O(10$  km) and hourly scale), precipitation is near-zero for  
<sup>291</sup> negative values and strongly increases above zero buoyancy, a behavior reminiscent of its exponen-  
<sup>292</sup> tial dependence on column moisture. The strength of this precipitation-buoyancy relationship lies  
<sup>293</sup> in its universality, as it holds over all tropical oceans, and, with slight modifications, over tropical  
<sup>294</sup> land (Ahmed et al. 2020). Using conditional averages reduces the scatter in precipitation rates  
<sup>295</sup> associated with a given value of  $B_L$ . This spread can be due to both stochasticity or ignored physical  
<sup>296</sup> effects, e.g. higher-order dependencies on the vertical structure of environmental temperature and  
<sup>297</sup> moisture, or wind shear effects. Figure 5 (second and fourth columns), shows the joint distribution  
<sup>298</sup> of precipitation and  $B_L$  for each region, using daily-mean data and regional averages. Spatially  
<sup>299</sup> averaging the nonlinear rainfall- $B_L$  relationship is expected to smooth out the sharp pickup around  
<sup>300</sup> zero buoyancy; hence, we show exponential fits (rather than ramp fits) with the joint distributions.  
<sup>301</sup> We also show conditional averages at various  $B_L$  values.  $B_L$  is more skillful than IVT<sub>⊥</sub> at capturing  
<sup>302</sup> daily rainfall variations in all regions except perhaps Myanmar, where the range of  $B_L$  is narrower  
<sup>303</sup> than in other regions (during the summer monsoon, the coast of Myanmar is in a precipitating state  
<sup>304</sup> most of the time). We next decompose variations in  $B_L$  into contributions from its components to  
<sup>305</sup> understand the origins of precipitation variability in tropical orographic regions.

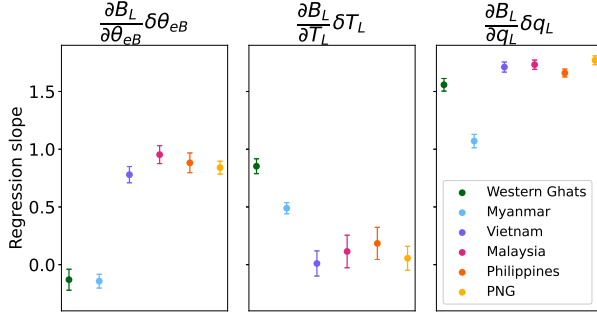
---

<sup>1</sup>Here, the boundary layer is defined as between the surface and 900 hPa, and the lower-free-troposphere between 900 hPa and 600 hPa. We chose these definitions (over using a fixed-depth boundary layer and variable-depth lower free troposphere) so that lower-free-tropospheric averages are not affected by surface elevation changes. Points where the surface pressure is lower than 900 hPa are masked out of all analyses.



282 FIG. 6. Joint distributions of buoyancy anomalies  $\delta B_L$  and their contribution from  $\theta_{eB}$  anomalies (first row),  $T_L$   
 283 anomalies (second row), and  $q_L$  anomalies (third row), for two regions illustrating different regimes: the Western  
 284 Ghats (left) and PNG (right). For each plot,  $\delta B_L$  is also regressed on the individual contribution  $(\partial B_L / \partial V) \delta V$   
 285 where  $V = \theta_{eB}, T_L$ , or  $q_L$ . Black dashed lines show the best fit linear regression.

306  $B_L$  is a function of three variables:  $\theta_{eB}, \theta_{eL}$ , and  $\theta_{eL}^*$  (eqn. 3). Alternatively, it can be viewed  
 307 as a function of  $\theta_{eB}, T_L$  and  $q_L$ , where  $T$  is temperature and  $q$  denotes specific humidity, hereafter  
 308 in temperature units (i.e. multiplied by the ratio of the latent heat of vaporization of water  
 309  $L_v$  to the heat capacity of air at constant pressure  $c_p$ ). In this description, plume buoyancy is  
 310 affected by boundary layer  $\theta_e$  (which affects lower-tropospheric stability), lower-free-tropospheric  
 311 temperature (affecting both stability and lower-free-tropospheric subsaturation) and lower-free-  
 312 tropospheric moisture (affecting only the subsaturation component). To evaluate the sensitivity of



286 FIG. 7. Regional variations in the slopes of linear regressions of  $\delta B_L$  against its individual contributions from  
 287  $\theta_{eB}$  anomalies (left),  $T_L$  anomalies (middle), and  $q_L$  anomalies (right) (see Fig. 6). Error bars show the 95%  
 288 confidence interval for these slopes. Note that the Western Ghats and Myanmar behave differently from other  
 289 regions, with  $T_L$  anomalies being more important than  $\theta_{eB}$  anomalies in setting  $B_L$  variations.

313  $B_L$  to each component, we linearize its expression:

$$\delta B_L = \frac{\partial B_L}{\partial \theta_{eB}} \delta \theta_{eB} + \frac{\partial B_L}{\partial T_L} \delta T_L + \frac{\partial B_L}{\partial q_L} \delta q_L \quad (4)$$

314 where  $\delta$  denotes a deviation from a time-average,  $\partial B_L / \partial \theta_{eB} = g w_B / \theta_{eL}^*$ , and the expressions for  
 315  $\partial B_L / \partial T_L$  and  $\partial B_L / \partial q_L$  are given in Ahmed et al. (2020) (these expressions were derived from a  
 316 simplified version of  $B_L$  that is very close to the one employed here). Here, we use fixed values of  
 317  $\partial B_L / \partial \theta_{eB} = 0.014$ ,  $\partial B_L / \partial T_L = -0.058$ , and  $\partial B_L / \partial q_L = 0.014$ , which have little dependence on  
 318 the specific base state considered.

319 Figure 6 examines the contribution of each term on the right-hand-side of (4) to variations in  
 320  $B_L$ , over the Western Ghats and PNG. For example, to estimate the contribution of  $\theta_{eB}$  variations  
 321 to  $B_L$  variations, we fix  $T_L$  and  $q_L$  and estimate the  $B_L$  perturbations that would have occurred  
 322 if only  $\theta_{eB}$  had varied, i.e.  $(\partial B_L / \partial \theta_{eB}) \delta \theta_{eB}$ . We regress  $\delta B_L$  on this measure and show the  
 323 joint distribution of both quantities. It is apparent from these distributions and the regression  
 324 fits that  $q_L$  dominates  $B_L$  variations in both regions. This is true even though  $B_L$  is four times  
 325 more sensitive to  $T_L$  ( $|\partial B_L / \partial T_L| \simeq 4 \partial B_L / \partial q_L$ ). Indeed, variations of  $q_L$  are less constrained than  
 326 those of  $T_L$ : lower-free-tropospheric temperature anomalies are quickly smoothed in the tropics by  
 327 gravity waves, resulting in a state of weak temperature gradients (e.g. Sobel et al. 2001). Over the  
 328 Western Ghats,  $T_L$  variations still account for 28% of the variance in  $B_L$ , while  $\theta_{eB}$  variations do not

342 TABLE 2. Correlations between daily precipitation (P) and the three quantities affecting plume buoyancy ( $\theta_{eB}$ ,  
 343  $T_L$  and  $q_L$ ), and between daily SST and boundary layer equivalent potential temperature  $\theta_{eB}$ . Precipitation,  $\theta_{eB}$ ,  
 344  $T_L$  and  $q_L$  are averaged over the red boxes in Fig. 3, and SST is averaged over the ocean part of each box.

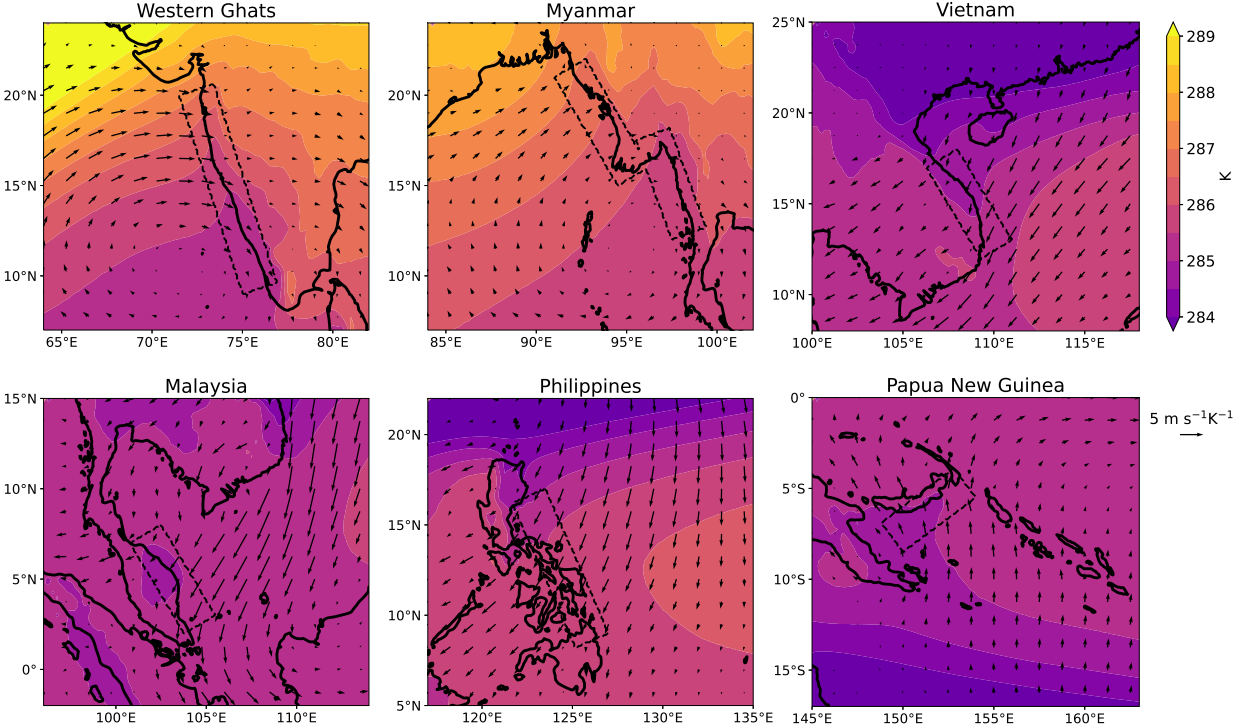
Region name	P - $\theta_{eB}$	P - $T_L$	P - $q_L$	SST- $\theta_{eB}$
Western Ghats	0.19	-0.15	0.56	0.80
Myanmar	0.16	-0.18	0.30	0.53
Vietnam	0.23	0.03	0.53	0.61
Malaysia	0.17	-0.18	0.51	0.69
Philippines	0.10	-0.08	0.50	0.52
PNG	0.15	-0.15	0.51	0.60

329 correlate with  $B_L$ . In PNG, the converse picture holds. Figure 7 shows the slopes of the regression  
 330 lines that appear in Fig. 6, extended to all regions. Although the sample size of six regions  
 331 is small, there seem to be two types of behavior: one where buoyancy variations are controlled  
 332 by lower-free-tropospheric thermodynamic quantities (the Western Ghats and Myanmar), and the  
 333 other where boundary layer  $\theta_e$  and lower-free-tropospheric moisture set these variations (Vietnam,  
 334 Malaysia, the Philippines, and PNG).

335 To link this analysis back to precipitation variations, we compute correlations between daily  
 336 values of rainfall and each of  $\theta_{eB}$ ,  $T_L$  and  $q_L$  upstream of each of the mountain ranges studied.  
 337 These correlations are only a crude measure of the association of each component with precipitation,  
 338 given that the precipitation-buoyancy relationship is expected to be nonlinear. Nevertheless, a few  
 339 of the observations made above hold:  $q_L$  has the strongest association with precipitation,  $T_L$   
 340 anomalies are negatively associated with precipitation (recall that  $\partial B_L / \partial T_L < 0$ ), and  $\theta_{eB}$  has a  
 341 weak positive association with rainfall.

345 *b. Controls on daily  $\theta_{eB}$  variations*

346 In this work, the boundary layer extends between the 900 hPa level and the surface—which  
 347 loosely corresponds to the subcloud layer. Boundary layer  $\theta_e$ , or equivalently subcloud entropy, is  
 348 set by exchanges with the surface and the lower free troposphere, with a small contribution from  
 349 radiative cooling (Emanuel et al. 1994). Entropy exchanges at the top of the boundary layer are  
 350 twofold: one contribution being in the form of quasi-continuous turbulent mixing across the top of  
 351 the layer, the other one arising from penetrative convective downdrafts. Over ocean, sea-surface



361 FIG. 8. Boundary layer horizontal wind regressed on lower-free-tropospheric temperature ( $T_L$ , averaged in  
 362 the dashed boxes). The result is multiplied by  $-1$  so that upslope flow is associated with negative temperature  
 363 perturbations. The color shading shows seasonal-mean  $T_L$ . Arrows are masked where neither the  $u$  wind  
 364 regression nor the  $v$  wind regression satisfy the false discovery rate criterion (Wilks 2016) with  $\alpha = 0.01$ .

352 temperature (SST) is often the dominant quantity affecting subcloud entropy (e.g. Lindzen and  
 353 Nigam 1987). Because the orographic rain bands of interest in this section are in close proximity  
 354 to the sea, one might expect SSTs to exert a strong control on  $\theta_{eB}$ . We verify this fact in table 2:  
 355 SST strongly correlates with  $\theta_{eB}$  at the daily scale, with correlation coefficients between 0.5 and  
 356 0.8 in all regions.

357 Other factors such as surface wind speed variations or convective downdrafts contribute to  
 358 variations in  $\theta_{eB}$  on shorter timescales than SST changes. Because there is no clear influence of  
 359 orographic mechanical forcing on any of these factors, we do not delve deeper into this topic.

360 *c. Controls on daily lower-free-tropospheric temperature variations*

365 Topographically forced gravity waves carry temperature perturbations. In the canonical picture  
 366 of mechanical orographic forcing, a mountain of height  $h_m$  is placed in a stratified atmosphere (with

buoyancy frequency  $N$ ) with a uniform background horizontal wind  $U$ . When the nondimensional mountain height  $Nh_m/U \lesssim 1$ , the flow ascends over the mountain, creating (by adiabatic cooling) a cold anomaly in the lower-free-troposphere upstream. The stronger the wind, the deeper the ascent region, hence the colder the anomaly. In the case of a Witch-of-Agnesi ridge of height 1 km, the sensitivity of the temperature perturbation to the impinging wind is (see Appendix)

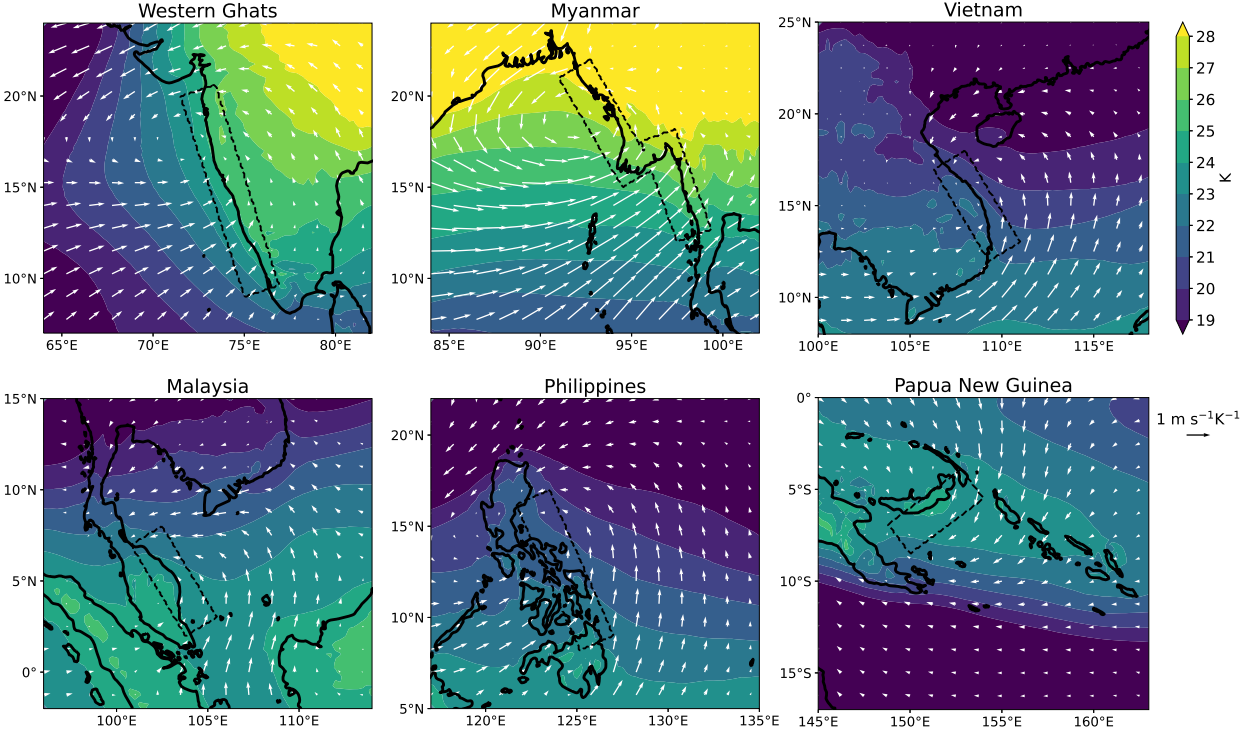
$$\frac{\partial T'_L}{\partial U} \simeq -0.2 \text{ K/(m s}^{-1}\text{).} \quad (5)$$

We now seek to verify whether  $T_L$  variations in our regions have patterns that are consistent with this picture. Figure 8 shows time-mean  $T_L$  maps in all six regions. A distinct cold anomaly (of around 0.5 K) is visible in each region's rain band, consistent with the idea of upstream cooling by orographic lifting in the mean state. To study temporal variations in the strength of this cool anomaly, we average  $T_L$  upstream of each mountain range to obtain daily timeseries. Because the mountains are of modest height in each region, we expect mountain waves to be dominantly affected by winds in the lowermost kilometer of the troposphere. We thus average horizontal winds within the boundary layer and regress them on the  $T_L$  timeseries at each location. The resulting wind vectors are multiplied by  $-1$  so that onshore cross-slope flow corresponds to negative temperature perturbations, and shown in Fig. 8. If our simple estimate (5) were to hold, regressed winds would have a magnitude around  $5 \text{ m s}^{-1}\text{K}^{-1}$  for a 1 km-high mountain.

The wind regressions are directed onshore and cross-slope in each region, which is again consistent with the idea that  $T_L$  is modulated by the strength of stationary mountain waves. Furthermore, the magnitude of the regression vectors upstream of each region (except Myanmar) is around  $2\text{-}5 \text{ m s}^{-1}\text{K}^{-1}$ , consistent with (5). It is apparent from Fig. 8 (especially in the Philippines, Vietnam, and PNG) that cold anomalies are also associated with up-temperature-gradient winds: background temperature gradients are not everywhere small in these tropical regions, and accordingly cooling can happen through horizontal advection.

#### *393 d. Controls on daily lower-free-tropospheric moisture variations*

Given the dominant control  $q_L$  exerts on lower tropospheric buoyancy (Fig. 6), understanding drivers of its temporal changes is key to understanding rainfall variations. In the same way they bear temperature anomalies, mountain waves carry moisture perturbations through vertical



383 FIG. 9. Boundary layer horizontal wind regressed on lower-free-tropospheric moisture ( $q_L$ , averaged in the  
 384 dashed boxes, in temperature units). The color shading shows seasonal-mean  $q_L$ . Arrows are masked using the  
 385 same criterion as in Fig. 8.

397 displacements in a background profile of specific humidity. Rising air upstream of a mountain  
 398 moistens the lower-free-troposphere, while downstream subsidence dries it. The magnitude of this  
 399 effect is estimated using linear mountain wave theory in the Appendix. In this idealized picture,  
 400 the sensitivity of the upstream moisture perturbation to the cross-slope wind is

$$\frac{\partial q'_L}{\partial U} \simeq 0.5 \text{ K}/(\text{m s}^{-1}). \quad (6)$$

401 Once again, this effect neglects any convective response: mountain-induced  $T_L$  and  $q_L$  perturbations  
 402 result in enhanced convection, which, in turn, dries the troposphere. A framework to understand  
 403 the response of convection to thermodynamic perturbations in a mountain wave is presented in  
 404 section 6. Solving for  $q'_L$  in this framework reduces the sensitivity in (6) by about half.

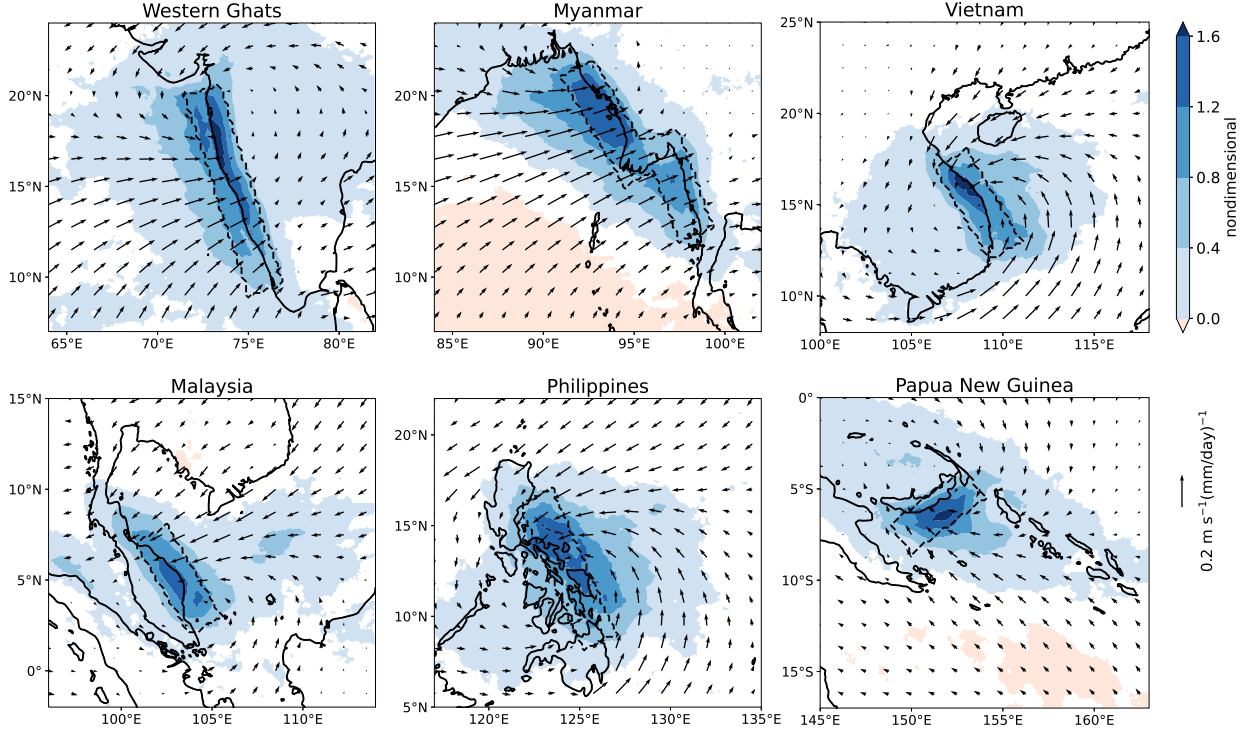
405 In the absence of horizontal gradients in the background moisture profile,  $q_L$  perturbations  
 406 would be dominantly due to mountain waves. In Earth's tropics however, water vapor is far from

being horizontally homogeneous. This is apparent in Fig. 9, where color shading represents the time-mean  $q_L$  in each region: horizontal moisture gradients are much stronger than  $T_L$  gradients. Although the impact of orography on the mean  $q_L$  distribution is less apparent compared to  $T_L$ , it seems to perturb moisture contours upstream of Myanmar, the Philippines, and PNG. In the presence of background moisture gradients, down-gradient winds are an efficient way to moisten the lower troposphere. Consequently, one may expect variations in  $q_L$  to be influenced by cross-gradient winds rather than cross-slope winds, contrary to temperature.

The vectors in Fig. 9 show horizontal winds regressed on upstream-averaged  $q_L$ . In the Western Ghats and Myanmar, moist perturbations are mostly associated with cross-slope winds, following the theoretical picture of mechanical forcing. The magnitude of the regressions ( $1\text{-}2 \text{ m s}^{-1}\text{K}^{-1}$ ) is somewhat smaller than expected from (6) - one would expect  $2\text{-}4 \text{ m s}^{-1}\text{K}^{-1}$  when accounting for the correction due to convective feedback (see above). The fact that both negative  $T_L$  and positive  $q_L$  perturbations—hence positive  $B_L$  perturbations—are favored by cross-slope winds in the Ghats and Myanmar explains why  $\text{IVT}_\perp$  characterizes precipitation better there than in other regions (Fig. 5).

In Vietnam, Malaysia, and the Philippines, regressed winds have little cross-slope flow component: they are mostly directed down mean moisture gradients. In these regions, moistening of the lower free troposphere thus seems to be more effectively attained through large-scale horizontal moisture advection than mechanical forcing of upslope flow. This result contrasts with the intuitive view that mechanically forced orographic precipitation and accompanying lower-tropospheric humidity variations are mostly controlled by forced ascent, i.e. by the strength of upslope flow. It shows that, despite its importance in setting the time-mean rainfall pattern, orographic forcing might be less important than large-scale horizontal moisture advection in setting the temporal variability of precipitation in these regions.

The regression pattern in PNG is neither cross-slope nor down-moisture-gradient. Indeed, the orographic rain band of PNG corresponds to a local maximum in lower-tropospheric specific humidity. Although we do not have a precise explanation for this pattern of wind anomalies, one may speculate that it is associated with large-scale upward motion in the South Pacific convergence zone (SPCZ), where PNG is located.



442 FIG. 10. Boundary layer horizontal wind regressed on precipitation averaged in the dashed boxes. The color  
 443 shading shows precipitation regressed on this same index. Masked arrows and white shading indicate that the  
 444 regressions do not satisfy the false discovery rate criterion with  $\alpha = 0.01$ .

446 We note that moistening of the lower troposphere is not solely controlled by horizontal winds, and  
 447 that any source of uplift, such as convectively coupled waves or cyclonic disturbances, will affect  
 448  $q_L$ . In this section we focused on horizontal wind control because horizontal winds dictate the  
 449 strength of uplift in stationary mountain waves, and are consequently a primary factor modulating  
 450 the effect of orography on  $q_L$  variations.

441 *e. Controls on daily precipitation variations*

445 To verify whether the same factors that govern lower-free-tropospheric temperature and moisture  
 446 control rainfall variations, we now regress horizontal wind on daily upstream precipitation in each  
 447 region (Fig. 10). Enhanced rainfall is associated with some amount of upslope flow in all regions,  
 448 confirming the importance of orographic mechanical forcing in influencing precipitation variability  
 449 there. Deviations from pure upslope flow (especially in Vietnam, Malaysia, the Philippines and  
 450 PNG) are consistent with the wind patterns that dictate  $q_L$  variations (see Fig. 9), i.e. down-

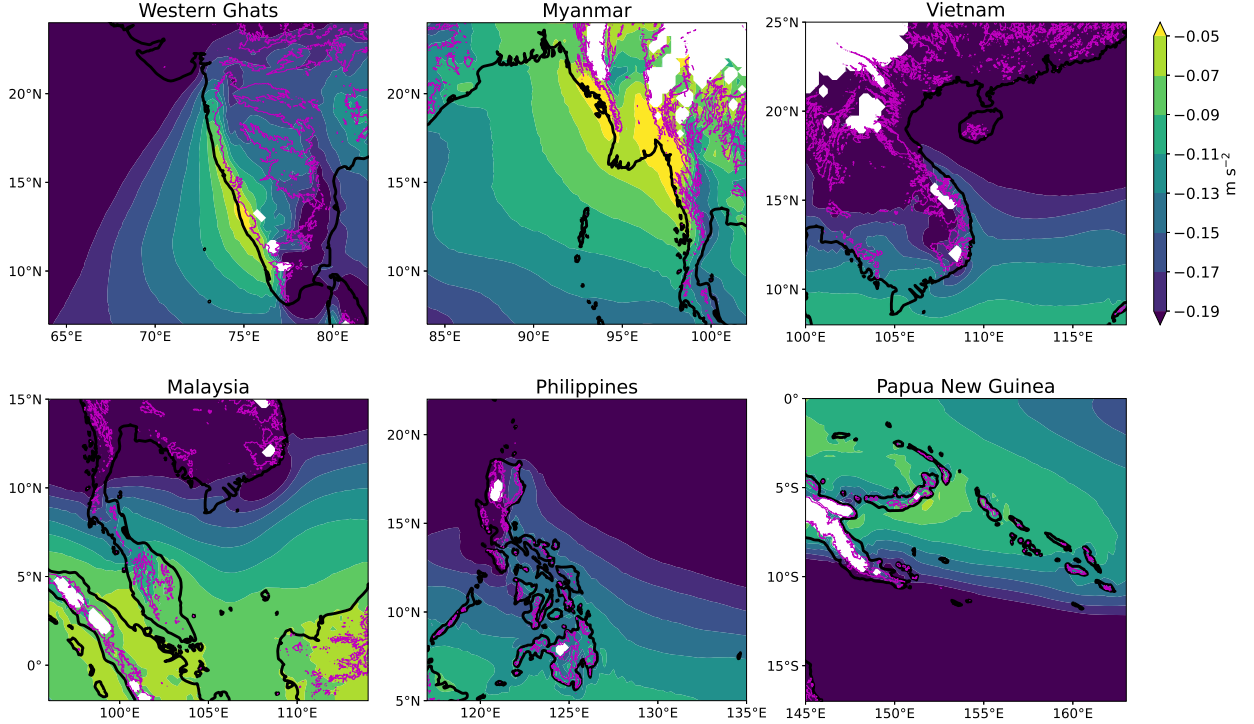
451 moisture gradient winds. This confirms the joint control of orographic lifting and large-scale  
452 moisture advection on orographic precipitation variability in the tropics.

453 Color shading in Fig. 10 shows precipitation regressed on this same upwind precipitation index.  
454 The existence of areas of weak positive association with the upwind rain index that are much  
455 wider than the orography indicate that orographic rainfall is partially controlled by large-scale,  
456 “background” precipitation variations. The stronger regression coefficients localized close to  
457 and preferentially upstream of the orography suggests the existence of an orographic mode of  
458 precipitation variability in each region. Patterns of positive association extend several hundred  
459 kilometers upstream of the regions used to define the rainfall index, as expected given the far-  
460 reaching influence of mechanical forcing upstream of a ridge (NB22).

## 461 5. Spatial distribution of buoyancy around orography

464 Large spatial gradients are an ubiquitous characteristic of orographic rainfall. All regions in  
465 Fig. 3 exhibit a windward rainfall peak and a leeward rain shadow less than 200 km apart, with  
466 seasonal-mean precipitation rates varying from more than  $15 \text{ mm day}^{-1}$  to less than  $5 \text{ mm day}^{-1}$   
467 on short distances. The buoyancy framework presented in section 4 naturally applies on short  
468 temporal scales, as buoyancy anomalies are consumed in a few hours (Ahmed et al. 2020). Here,  
469 we explore its potential to explain precipitation patterns on much longer time scales. Specifically,  
470 we explore whether seasonal-mean spatial features of orographic precipitation follow the spatial  
471 distribution of time-averaged buoyancy  $B_L$ .

472 The precipitation- $B_L$  relationship was initially introduced as a nonlinear statistical relationship  
473 holding at short spatial and small temporal scales (Ahmed and Neelin 2018). It is statistical in  
474 the sense that a single value of  $B_L$  corresponds to a range of precipitation rates - the relationship  
475 appears when conditionally averaging precipitation. Taking time averages is thus favorable in that  
476 it eliminates the underlying stochasticity. However, averaging over a nonlinear relationship may  
477 yield a non-unique mapping between time-mean precipitation  $\bar{P}$  and time-mean buoyancy  $\bar{B}_L$ . For  
478 example, it appears from Fig. 5 that the orographic rain band upstream of Myanmar has a narrower  
479 distribution of  $B_L$  than other regions. This suggests that  $\bar{B}_L$  values in that region may be higher  
480 than in other places with comparable rain rates, e.g. upstream of the Western Ghats or PNG.



462 FIG. 11. Maps of seasonal-mean plume buoyancy  $B_L$ . The 500 m topography contour is shown in magenta.  
 463 White shading represents undefined  $B_L$  values, wherever the surface pressure is lower than 900 hPa.

481 Nonetheless, one might still expect that monotonic relationship between  $\overline{B_L}$  and  $\overline{P}$ , perhaps with  
 482 variations across regions.

483 We compute  $B_L$  from ERA5 temperature and moisture data at  $0.25^\circ$  and daily resolution, then  
 484 average temporally over each region's rainiest season for 20 years. The resulting maps are shown in  
 485 Fig. 11. Spatial features on these maps are broadly consistent with the maps of mean precipitation  
 486 in Fig. 3. A distinct peak is visible upwind of each orographic barrier, with decreased  $B_L$  values  
 487 in the lee: this confirms that mechanical forcing spatially distributes precipitation in a manner  
 488 consistent with its effect on the temperature and moisture fields. This effect was already noted in  
 489 Section 4 in the maps of time-averaged  $T_L$  and  $q_L$  (Figs. 8 and 9, where upstream cold anomalies  
 490 were present in all regions, and moist anomalies in several regions).  $B_L$  peaks are collocated  
 491 with rainfall peaks (see Fig. 3) in all regions except Myanmar: interestingly, the easternmost  $B_L$   
 492 peak extends 200 km inland, whereas the rainfall peak follows the east-west coastline at  $16^\circ\text{N}$ .  
 493 The reasons for the precipitation maxima to follow the coast rather than the topography there  
 494 are unknown, and suggests that the land-ocean contrast may play an important role in organizing

495 rainfall in this region otherwise dominated by mechanical forcing. We note, however, that the ERA5  
496 precipitation distribution (not shown) follows the  $B_L$  pattern, with lower values than IMERG along  
497 the east-west coastline and higher values inland. This may indicate that the reanalysis does not  
498 accurately represent the underlying  $B_L$  distribution there.

499 Except for the special case of Myanmar, rain shadows are consistent with the time-mean buoy-  
500 ancy distribution. Reduced values of  $B_L$ , mostly associated with a warmer and/or drier lower-  
501 troposphere, are visible downstream of the mountain ranges, consistent with the expected effect of  
502 gravity wave subsidence there. In the Western Ghats and in PNG,  $B_L$  does not drop as sharply as  
503 precipitation downstream of the rainfall maximum. Once again, ERA5 precipitation (not shown)  
504 partly reflects this fact, with overestimated rainfall values especially downstream of PNG. This  
505 could mean that ERA5 underestimates the warm and dry anomalies resulting from mechanically  
506 forced subsidence there (perhaps because the topography is under-resolved). Alternatively, the  
507  $B_L$  framework may only partially account for the suppression of precipitation in rain shadows.  
508 Convection may be affected by higher-order variations in the vertical structures of temperature and  
509 moisture, or by neglected dynamical effects (e.g., mountain lees are regions of strong wind shear).

## 510 **6. A linear model for seasonal-mean tropical orographic precipitation**

511 Section 5 suggests that the spatial organization of tropical orographic rainfall is adequately  
512 captured by the time-mean plume buoyancy distribution. However, we have yet to quantify the  
513 effect of orography on this distribution. Here, we delve further into the physical drivers through  
514 which orography influences  $B_L$  and sets the strength and location of rainfall peaks and rain shadows.  
515 We use a simple theory that solves, for any topographic shape, the time-mean temperature and  
516 moisture anomalies carried by a stationary mountain wave (including convective feedback on the  
517 moisture anomalies) to estimate the time-mean precipitation distribution. We compare the results  
518 with observations and with two existing theories for mechanically forced orographic rainfall.

### 519 *a. Derivation*

520 The theory we present closely follows the one developed in NB22, but extends it to two horizontal  
521 dimensions. We give an outline of the derivation, and refer readers to that work for more details.  
522 A low-latitude domain with topography  $h(x, y)$  has a constant background wind  $\mathbf{u}_0 = (u_0, v_0)$  and

523 Brunt-Väisälä frequency  $N$ . The flow is decomposed as the sum of a basic state, a “dry” mode (that  
 524 carries temperature and moisture perturbations from a stationary mountain wave), and a “moist”  
 525 mode (that consists of a convective response to these perturbations). The dry mode influences  
 526 the moist mode by altering convective heating and moistening, that are parameterized as functions  
 527 of lower-tropospheric temperature and moisture following the  $B_L$  framework, but the moist mode  
 528 does not affect the dry mode. In this section only, temperature and moisture are in energy units  
 529 (compared to the previous sections, they are multiplied by  $c_p$ ), for consistency with NB22.

530 Steady-state thermodynamic and moisture equations for the moist mode read:

$$\mathbf{u}_0 \cdot \nabla T_m + \omega_m \frac{ds_0}{dp} = Q_c - R, \quad (7a)$$

$$\mathbf{u}_0 \cdot \nabla q_m + \omega_m \frac{dq_0}{dp} = Q_q + E, \quad (7b)$$

531 where  $s_0(p)$  and  $q_0(p)$  are the background dry static energy profile and moisture profile (in energy  
 532 units).  $Q_c$  and  $Q_q$  denote convective heating and moistening, while  $R$  and  $E$  are radiative cooling  
 533 and surface evaporation rates.  $\omega$  is the pressure velocity, and the subscript  $m$  is used for moist  
 534 mode quantities (we will similarly use a subscript  $d$  for dry mode properties).

535 We use the weak temperature gradient approximation for the moist mode, which implies that  
 536  $T_m$  is horizontally uniform; this allows us to set  $T_m = 0$ . Truncating the vertical velocity profile  
 537 as  $\omega_m(x, y, p) = \omega_1(x, y)\Omega(p)$ , where  $\Omega$  is a first-baroclinic-mode profile, and vertically averaging  
 538 over the depth of the troposphere yields

$$-\omega_1 M_s = \langle Q_c \rangle - \langle R \rangle, \quad (8a)$$

$$\mathbf{u}_0 \cdot \nabla \langle q_m \rangle + \omega_1 M_q = \langle Q_q \rangle + \langle E \rangle, \quad (8b)$$

539 where  $M_s = -\langle \Omega \partial s_0 / \partial p \rangle$ ,  $M_q = \langle \Omega \partial q_0 / \partial p \rangle$ , and  $\langle \cdot \rangle$  denotes a vertical average in pressure coor-  
 540 dinates.  $M = M_s - M_q$  is known as the gross moist stability, and  $M/M_s$  as the normalized gross  
 541 moist stability (NGMS, Raymond et al. 2009).

542 Following Ahmed et al. (2020), the precipitation- $B_L$  relationship is linearized (and boundary-  
 543 layer  $\theta_e$  is assumed constant) - which yields

$$\langle Q_c \rangle = \frac{q'_L}{\tau_q} - \frac{T'_L}{\tau_T} = \frac{q_{dL} + q_{mL}}{\tau_q} - \frac{T_{dL}}{\tau_T}, \quad (9)$$

544 where  $q_{dL}$  and  $q_{mL}$  are lower-free-tropospheric moisture perturbations carried by the dry and moist  
 545 modes,  $T_{dL}$  is the dry mode temperature perturbation (recall  $T_m = 0$ ), and the convective time scales  
 546  $\tau_T$  and  $\tau_q$  are constants appearing from the linearization. For seasonal-mean rainfall, these are  
 547 taken as  $\tau_T = 7.5$  hr and  $\tau_q = 27.5$  hr, a factor 2.5 higher than their values when used to represent  
 548 precipitation at the hourly scale. Because the vertical structure of moisture is horizontally uniform,  
 549  $q_{mL}$  and  $\langle q_m \rangle$  are proportional to each other; we therefore define an adjustment time scale for  
 550 vertically averaged moisture,  $\tilde{\tau}_q = 0.6\tau_q$  such that  $q_{mL}/\tau_q = \langle q_m \rangle/\tilde{\tau}_q$ .

551 We now use conservation of energy to relate convective heating, moistening, and precipitation  
 552 by

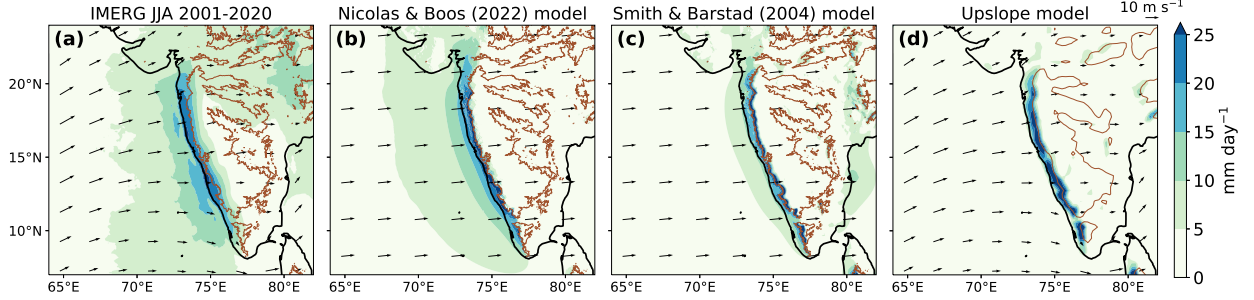
$$\langle Q_c \rangle = -\langle Q_q \rangle = \frac{\rho_w L_v g}{p_T} P, \quad (10)$$

553 where  $p_T = 800$  hPa is the depth of the troposphere and  $\rho_w = 1000 \text{ kg m}^{-3}$  is the density of water.  
 554 The first factor on the right-hand-side converts a precipitation rate (in  $\text{m s}^{-1}$  or  $\text{mm day}^{-1}$ ) into a  
 555 convective heating rate (in  $\text{J kg}^{-1} \text{s}^{-1}$ ). We henceforth define  $\beta = p_T/(\rho_w L_v g)$ . Using this definition  
 556 and combining (8a), (8b), (9), and (10), we derive an equation for  $P$ :

$$\mathbf{u}_0 \cdot \nabla P + \frac{\text{NGMS}}{\tilde{\tau}_q} (P - P_0) = \beta \mathbf{u}_0 \cdot \nabla \left( \frac{q_{dL}}{\tau_q} - \frac{T_{dL}}{\tau_T} \right), \quad (11)$$

559 where  $P_0 = \beta \frac{M_s \langle E \rangle - M_q \langle R \rangle}{M}$  is a background rain rate. The right-hand-side of equation (11)  
 560 represents a forcing of convection by the dry mode. The second term on the left-hand-side  
 561 represents convective relaxation: precipitation forced by the cool and moist perturbations of  
 562 the dry mode dries the lower-free-troposphere, which in turn relaxes rainfall back towards the  
 563 background rate  $P_0$ . The reverse process happens when precipitation is suppressed by warm and  
 564 dry perturbations. This process happens on a length scale  $L_q = \tilde{\tau}_q |\mathbf{u}_0| / \text{NGMS}$ .

565 Solving for  $T_{dL}$  and  $q_{dL}$  using mountain wave theory allows us to map a given topographic shape  
 566 to the associated precipitation distribution using a Fourier transform. In the dry mode, moisture is



557 FIG. 12. Maps of mean precipitation in the Western Ghats. (a) Observations (IMERG V06B), (b) Nicolas and  
558 Boos (2022) theory, (c) Smith and Barstad (2004) theory, (d) upslope model ( $\text{IVT} \cdot \nabla h / H_{\text{sat}}$ ).

567 conserved and there are no diabatic processes. Hence, horizontal advection terms are balanced by  
568 vertical advection:

$$\mathbf{u}_0 \cdot \nabla \left( \frac{q_{dL}}{\tau_q} - \frac{T_{dL}}{\tau_T} \right) = w_{dL} \left( \frac{1}{\tau_T} \frac{ds_0}{dz} - \frac{1}{\tau_q} \frac{dq_0}{dz} \right), \quad (12)$$

569 where  $w_{dL}$  is the vertical velocity of the dry mode (we use height coordinates in the spirit of linear  
570 mountain wave theory). We define

$$\chi = \beta \left( \frac{1}{\tau_T} \frac{ds_0}{dz} - \frac{1}{\tau_q} \frac{dq_0}{dz} \right) \quad (13)$$

571 and substitute (12) into (11), which becomes (defining  $P' = P - P_0$ )

$$\mathbf{u}_0 \cdot \nabla P' + \frac{NGMS}{\tilde{\tau}_q} P' = \chi w_{dL}. \quad (14)$$

572 Here,  $w_{dL}$  is given by linear mountain wave theory, in two horizontal dimensions under the  
573 Boussinesq approximation, by (Smith 1979):

$$\hat{w}_d(k_x, k_y, z) = i\sigma \hat{h}(k_x, k_y) e^{im(k_x, k_y)z} \quad (15)$$

574 where  $k_x$  and  $k_y$  are the horizontal wavenumbers, hats denote Fourier transforms, and  $\sigma = k_x u_0 +$   
 575  $k_y v_0$ . Defining  $K^2 = k_x^2 + k_y^2$ , the vertical wavenumber  $m(k_x, k_y)$  is

$$m = \begin{cases} \operatorname{sgn}(\sigma) \sqrt{K^2 \left( \frac{N^2}{\sigma^2} - 1 \right)} & \text{if } \sigma^2 < N^2 \\ i \sqrt{K^2 \left( 1 - \frac{N^2}{\sigma^2} \right)} & \text{if } \sigma^2 > N^2 \end{cases}. \quad (16)$$

576 Fourier-transforming (14) and using (15) gives a closed expression for the Fourier-transformed  
 577 precipitation anomaly  $\hat{P}'$ :

$$\hat{P}'(k_x, k_y) = \frac{i\sigma\chi}{i\sigma + \frac{NGMS}{\tau_q}} \hat{h}(k_x, k_y) \left[ e^{im(k_x, k_y)z} \right]_L. \quad (17)$$

578 The main controlling parameters are topography  $h(x)$ , background wind  $u_0$ , stratification  $N$  and  
 579 a background moisture lapse rate. We note that in this model, the lower-troposphere is defined  
 580 between 1 km and 3 km above sea level. We now apply this model to the real-world tropics.

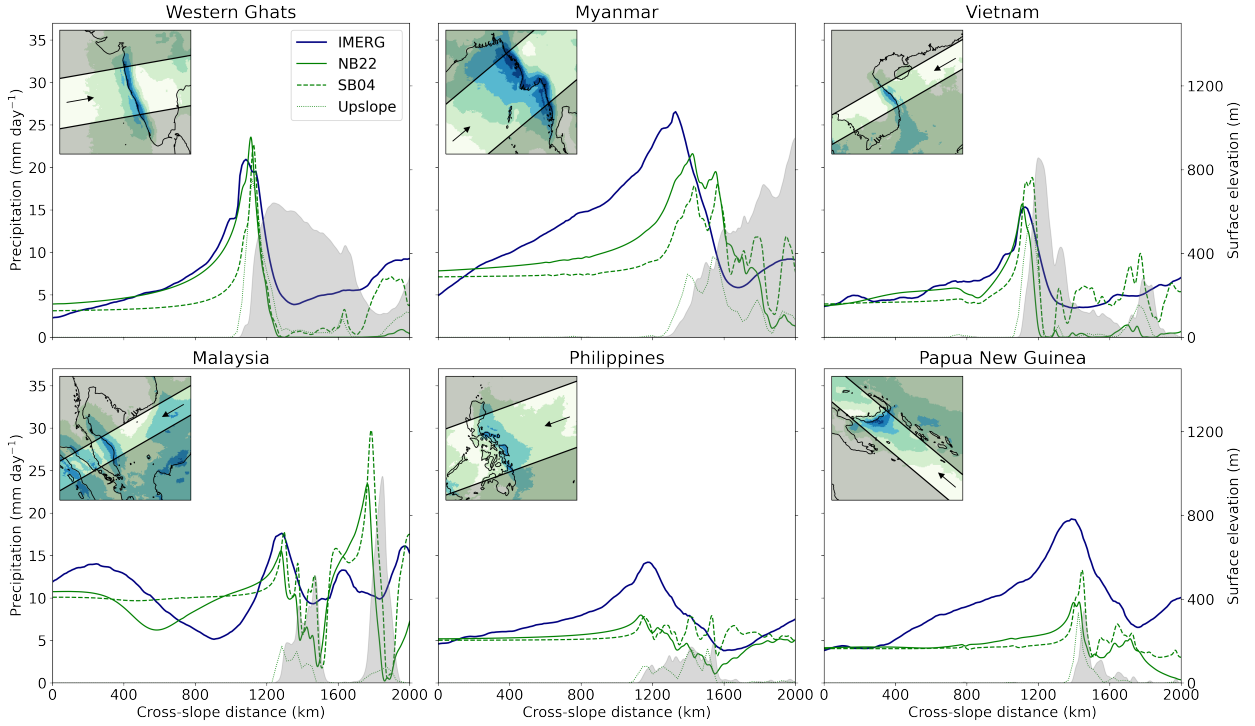
### 581 *b. Comparing observed and modeled rainfall distributions*

582 The ingredients comprising the above theory (weak temperature gradient approximation,  
 583 quasiequilibrium precipitation closure) make it especially suited to tropical regions. SB04 de-  
 584 veloped a model of mechanically forced orographic rainfall for convectively stable flows that has  
 585 been used to represent midlatitude orographic precipitation. Their model assumes that condensa-  
 586 tion results from ascent in a saturated atmosphere (see eq. 1). Vertical motion is computed using  
 587 linear mountain wave theory, and the effects of finite hydrometeor growth times and downwind  
 588 advection are parameterized. The fundamental difference between the models of SB04 and NB22  
 589 is the mechanism linking mountain waves to precipitation: in the former, rain is associated with  
 590 the ascent rate  $w$ , while in the latter, it is associated with vertical displacement of the lower-  
 591 free-troposphere from a background state. This results in shorter length scales for the upstream  
 592 enhancement of rainfall and rain shadows in SB04's model.

593 We compare observed and modeled seasonal-mean rainfall maps in the Western Ghats in Fig.  
 594 12<sup>2</sup>. Both the SB04 and NB22 models use a uniform static stability; we choose  $N = 0.01 \text{ s}^{-1}$ .

---

<sup>2</sup>For both models, the domain shown in Fig. 12 is padded to a square domain of side length 7500 km, with topography smoothed down to zero elevation 100 km outside of the main domain.



582 FIG. 13. Cross-sections of observed and modeled precipitation in all regions, along the direction of the  
 583 seasonal-mean wind. The insets show the orientation and width of the areas used to define cross sections (the  
 584 background shows mean observed precipitation as in Fig. 3). The gray shadings represent topography. The dark  
 585 blue lines are observed (IMERG) mean precipitation during each region's rainiest season. The green lines show  
 586 precipitation from the Nicolas and Boos (2022) theory (solid), the Smith and Barstad (2004) theory (dashed),  
 587 and the upslope model (dotted).

601 The background wind and precipitation rate are given in table 3. For the SB04 model, we use a  
 602 moist adiabatic lapse rate  $\Gamma_m = 4.3 \text{ K km}^{-1}$ , and hydrometeor growth and fallout times of 2000  
 603 s. To account for non-precipitating times, the SB04 precipitation rates are divided by a factor  
 604 2.5. For the NB22 model, we choose a lower-tropospheric moisture lapse rate of  $-8 \text{ K km}^{-1}$  and  
 605 NGMS = 0.2, representative of all the regions studied herein. Both theories (Fig. 12, panels b and  
 606 c) produce an upstream precipitation peak that is commensurate with observations (around 20 mm  
 607 day<sup>-1</sup>). As explained above, precipitation enhancement happens much closer to the ridge in the  
 608 SB04 model, which fails to account for high precipitation rates over the Arabian sea upstream of  
 609 the Western Ghats. It also predicts a second rainfall peak downstream, by the eastern coast of India,  
 610 associated with vertical motion predicted by linear mountain wave theory there. This is unlike the

611 NB22 model which features an extensive rain shadow. Although central and northeastern India do  
612 receive precipitation during summer (panel a), this is commonly thought to arise from the dynamics  
613 of synoptic-scale disturbances such as monsoon depressions (Sikka 1977) rather than mountain  
614 wave ascent downstream of the Indian topography.

615 For reference, Fig. 12 (panel d) shows precipitation from the upslope model (eq. 2). We convert  
616 the condensation rate into a precipitation rate using an efficiency factor  $\epsilon = 0.25$ . We use  $0.25^\circ \times$   
617  $0.25^\circ$  topography, as higher resolutions lead to unrealistic small-scale features in this model.  
618 Because it only predicts precipitation above mountain slopes, it does not account for any upstream  
619 rainfall enhancement. The above choice of precipitation efficiency yields a correct estimate for the  
620 peak precipitation magnitude, but this does not generalize to other regions (see below).

621 We extend this analysis to all regions, and show cross-sectional averages of the observed and  
622 modeled mean precipitation rates in Fig. 13. The insets show the direction and width of the cross  
623 sections, which were chosen normal to topography and following the prevailing wind direction.  
624 Background wind speeds and precipitation rates are listed in Table 3. With the fixed precipitation  
625 efficiency  $\epsilon = 0.25$  that produced a match to the peak precipitation magnitude in the Western Ghats,  
626 the upslope model greatly underestimates peak precipitation rates in nearly all other regions. Thus,  
627 in addition to missing the upstream enhancement of precipitation, this model requires region-  
628 specific tuning to yield accurate peak rainfall rates. The SB04 and NB22 models produce similar  
629 peak rain rates in all regions, differing primarily in the upstream extent of the orographic rainfall  
630 enhancement and in the leeside precipitation rates. The NB22 accurately predicts the rainfall  
631 enhancement upstream of certain regions (especially the Western Ghats and Vietnam), contrary to  
632 the stable-ascent model of SB04 that underestimates it everywhere. The description of orographic  
633 rainfall as the result of forced temperature and moisture perturbations in a lower-tropospheric  
634 quasiequilibrium state is thus consistent with observations there. In other regions (most notably  
635 the Philippines and PNG), both models greatly underestimate precipitation rates compared to  
636 observations. In the NB22 model, this failure results from an underestimation of the moisture  
637 anomaly  $q'_L$  (not shown). We speculate that positive  $q_L$  perturbations are not only the result of  
638 orographic lifting in these regions, and that climatological mean large-scale ascent, forced by  
639 non-orographic factors, plays a key role in producing the observed rainfall patterns. The fact that  
640 PNG is located within the SPCZ is consistent with this hypothesis.

TABLE 3. Parameters used in the precipitation models of Smith and Barstad (2004) and Nicolas and Boos (2022)

Region name	$u_0$ (m s $^{-1}$ )	$v_0$ (m s $^{-1}$ )	$P_0$ (mm day $^{-1}$ )
Western Ghats	10	1	3
Myanmar	8	8	7
Vietnam	-7	-5	4
Malaysia	-7	-5	10
Philippines	-8.5	-3	5
PNG	-7.5	5.5	4

641 Differences between observed and modeled precipitation rates are also apparent downstream  
 642 of the mountain ranges. The NB22 model seems to strongly overestimate the drying effect of  
 643 orography there. The main reason for this flaw is that the model assumes a time-independent  
 644 background wind, which leads the lee of mountains to be persistently warm and dry. In reality,  
 645 some days exhibit reversed flow or have a stronger along-slope component, creating more favorable  
 646 conditions for convection in the lee. Additionally, synoptic disturbances (such as monsoon de-  
 647 pressions downstream of the Indian subcontinent) may occasionally propagate into these regions,  
 648 contributing to small positive seasonal-average precipitation there. As explained above in the case  
 649 of the Western Ghats, the SB04 model predicts higher leeside precipitation rates, because linear  
 650 mountain wave solutions produce ascent there. This leads to localized downstream precipitation  
 651 peaks that are not seen in observations.

## 652 7. Discussion and conclusions

653 The spatial and temporal distribution of mechanically forced orographic rainfall is investigated in  
 654 six tropical regions. We show that a buoyancy proxy, evaluated from reanalysis data, captures many  
 655 aspects of both daily variations and the seasonal-mean spatial distribution of rainfall in all regions.  
 656 In this framework, the interaction of orography with the background wind creates temperature and  
 657 moisture anomalies in the lower troposphere, affecting the buoyancy of convective plumes and  
 658 thereby controlling precipitation.

659 This work confirms the important role of lower-free-tropospheric moisture ( $q_L$ ) in controlling  
 660 temporal variations in orographic convection. In the absence of background horizontal moisture  
 661 gradients,  $q_L$  variations would be fully controlled by orographic uplift, hence primarily by the  
 662 cross-slope wind speed. The presence of large-scale  $q_L$  gradients leads alternate directions of wind

anomalies to favor rainfall in some regions, namely down-moisture-gradient winds. Fluctuations in boundary-layer equivalent potential temperature also exert a secondary control on precipitation in most regions, and are not clearly linked to mechanical orographic forcing. These results indicate that mechanical forcing only exerts a partial control on rainfall variations in the regions studied.

Despite the nonlinear relationship between plume buoyancy  $B_L$  and precipitation, time-averaged  $B_L$  captures many spatial features of observed seasonal-mean precipitation maps. Discrepancies appear in the rain shadows, where  $B_L$  (as estimated from a reanalysis) overestimates precipitation. This points to a possible limitation of the present framework, in which convective dynamics are assumed identical over oceans and in mountains, with mountains only affecting plume buoyancy. Nevertheless, our goal here is to provide a first-order understanding of the mechanisms governing tropical orographic precipitation. We recognize that this approach neglects the influence on convection of some aspects of orographic dynamics, such as strong wind shears and gravity wave breaking.

We present a linear theory that predicts the time-mean rainfall distribution for arbitrary 2D topography and uniform wind. It quantifies the lower-tropospheric temperature and moisture perturbations caused by stationary mountain waves, and takes into account the feedback of convection on the moisture distribution. The theory accurately predicts upstream rainfall in some regions, especially the Western Ghats and Vietnam. In other regions (mainly the Philippines and Papua New Guinea), it yields weaker peak rainfall than observations. It is likely that mechanical forcing alone cannot explain the strong rain bands observed there. The presence of climatological-mean ascent, due to non-orographic factors (such as the SPCZ in Papua New Guinea), plays a key role in setting the lower-tropospheric moisture gradients, hence the rainfall patterns, in these regions.

685 *Acknowledgments.* This material is based on work supported by the U.S. Department of Energy,  
686 Office of Science, Office of Biological and Environmental Research, Climate and Environmental  
687 Sciences Division, Regional and Global Model Analysis Program, under Award DE-SC0019367.  
688 It used resources of the National Energy Research Scientific Computing Center (NERSC), which  
689 is a DOE Office of Science User Facility.

690 *Data availability statement.* The code containing linear precipitation models and that used in  
691 producing the figures will be archived at Zenodo, with a DOI issued once the review process  
692 and any needed revisions are complete. IMERG V06B, ERA5, and ETOPO1 data are publicly  
693 accessible online.

## APPENDIX

### 695 Lower-tropospheric temperature and moisture perturbations forced by an ideal mountain 696 ridge

697 We consider an infinite two-dimensional ( $x$ - $z$ ) domain whose surface height is

$$h(x) = h_m \frac{l_0^2}{x^2 + l_0^2}, \quad (\text{A1})$$

698 where  $l_0$  is the mountain half-width and  $h_m$  is the maximum height. This so-called Witch-of-Agnesi  
699 topography has a convenient Fourier transform, which renders the treatment of mountain wave  
700 solutions analytically tractable. The background horizontal wind speed  $U$  and static stability  $N$  are  
701 supposed uniform. We now estimate mechanically forced temperature perturbations using linear  
702 mountain wave theory, which is approximately valid under the assumption of small nondimensional  
703 mountain height  $Nh_m/U$ . Queney (1948) gives an analytical solution for  $\zeta(x, z)$ , the vertical  
704 displacement at  $x$  of a streamline originating upstream at  $z$ :

$$\zeta(x, z) = h_m \frac{\cos(Nz/U)l_0^2 - \sin(Nz/U)l_0x}{x^2 + l_0^2}. \quad (\text{A2})$$

705 This expression is valid when  $l_0N/U \gg 1$ , which is largely satisfied with a half-width  $l_0 \simeq 100$   
706 km,  $U \simeq 10 \text{ m s}^{-1}$ , and  $N \simeq 0.01 \text{ s}^{-1}$ . With uniform static stability, and in the absence of diabatic  
707 processes, a parcel lifted by  $\zeta$  experiences a cooling of magnitude  $\zeta ds_0/dz$ . Thus, the lower-free-

708 tropospheric temperature perturbation is

$$T'_L(x) = -h_m \frac{ds_0}{dz} \frac{\alpha_c l_0^2 - \alpha_s l_0 x}{x^2 + l_0^2}, \quad (\text{A3})$$

709 where  $\alpha_c = [\cos(Nz/U)]_L$ ,  $\alpha_s = [\sin(Nz/U)]_L$ , and  $[\cdot]_L$  denotes a lower-tropospheric average.  
710  $s_0(z)$  is the background dry static energy profile profile (divided by  $c_p$ ). Minimizing (A3) gives  
711 the peak lower-tropospheric temperature perturbation:

$$T'_{L,\max} = -h_m \frac{ds_0}{dz} \left( \sqrt{\alpha_c^2 + \alpha_s^2} + \alpha_c \right), \quad (\text{A4})$$

712 Evaluating  $\partial T'_{L,\max}/\partial U$  with a 1-km high mountain and  $N = 0.01 \text{ s}^{-1}$  gives (5).

713 The peak moisture perturbation is given by the same expression as (A4), replacing  $-ds_0/dz$  with  
714  $dq_0/dz$  (where  $q_0(z)$  is a background moisture profile). Using a lower-free-tropospheric moisture  
715 lapse rate representative of our regions ( $8 \text{ K km}^{-1}$ ), we obtain (6).

## 716 References

- 717 Ahmed, F., Á. F. Adames, and J. D. Neelin, 2020: Deep convective adjustment of temperature and  
718 moisture. *Journal of the Atmospheric Sciences*, **77** (6), 2163 – 2186, <https://doi.org/10.1175/JAS-D-19-0227.1>.
- 719
- 720 Ahmed, F., and J. D. Neelin, 2018: Reverse engineering the tropical precipitation–buoyancy  
721 relationship. *Journal of the Atmospheric Sciences*, **75** (5), 1587 – 1608, <https://doi.org/10.1175/JAS-D-17-0333.1>.
- 722
- 723 Amante, C., and B. Eakins, 2008: Etopo1 1 arc-minute global relief model: Procedures, data  
724 sources and analysis. *NOAA Technical Memorandum NESDIS NGDC-24. National Geophysical  
725 Data Center, NOAA*, <https://doi.org/10.7289/V5C8276M>, accessed 10 Sep 2022.
- 726
- 727 Anber, U., S. Wang, and A. Sobel, 2014: Response of atmospheric convection to vertical wind shear:  
728 Cloud-system-resolving simulations with parameterized large-scale circulation. part i: Specified  
radiative cooling. *Journal of the Atmospheric Sciences*, **71** (8), 2976 – 2993, <https://doi.org/10.1175/JAS-D-13-0320.1>.
- 729

- 730 Bagtasa, G., 2020: Influence of madden–julian oscillation on the intraseasonal variability of  
731 summer and winter monsoon rainfall in the philippines. *Journal of Climate*, **33** (22), 9581 –  
732 9594, <https://doi.org/10.1175/JCLI-D-20-0305.1>.
- 733 Biasutti, M., S. E. Yuter, C. D. Burleyson, and A. H. Sobel, 2012: Very high resolution rainfall pat-  
734 terns measured by TRMM precipitation radar: seasonal and diurnal cycles. *Climate Dynamics*,  
735 **39** (1), 239–258, <https://doi.org/10.1007/s00382-011-1146-6>.
- 736 Bretherton, C. S., M. E. Peters, and L. E. Back, 2004: Relationships between water vapor path and  
737 precipitation over the tropical oceans. *Journal of Climate*, **17** (7), 1517 – 1528, <https://doi.org/>  
738 [10.1175/1520-0442\(2004\)017<1517:RBWVPA>2.0.CO;2](https://doi.org/10.1175/1520-0442(2004)017<1517:RBWVPA>2.0.CO;2).
- 739 Chang, C.-P., Z. Wang, J. McBride, and C.-H. Liu, 2005: Annual cycle of southeast asia—maritime  
740 continent rainfall and the asymmetric monsoon transition. *Journal of Climate*, **18** (2), 287 – 301,  
741 <https://doi.org/10.1175/JCLI-3257.1>.
- 742 Chen, T.-C., J.-D. Tsay, M.-C. Yen, and J. Matsumoto, 2012: Interannual variation of the late  
743 fall rainfall in central vietnam. *Journal of Climate*, **25** (1), 392–413, <https://doi.org/10.2307/>  
744 [26191517](https://doi.org/10.2307/26191517).
- 745 Chen, T.-C., J.-D. Tsay, M.-C. Yen, and J. Matsumoto, 2013: The winter rainfall of malaysia.  
746 *Journal of Climate*, **26** (3), 936 – 958, <https://doi.org/10.1175/JCLI-D-12-00174.1>.
- 747 Connor Nelson, T., J. Marquis, J. M. Peters, and K. Friedrich, 2022: Environmental controls on  
748 simulated deep moist convection initiation occurring during relampago-cacti. *Journal of the*  
749 *Atmospheric Sciences*, **79** (7), 1941 – 1964, <https://doi.org/10.1175/JAS-D-21-0226.1>.
- 750 Derbyshire, S. H., I. Beau, P. Bechtold, J.-Y. Grandpeix, J.-M. Piriou, J.-L. Redelsperger, and  
751 P. M. M. Soares, 2004: Sensitivity of moist convection to environmental humidity. *Quarterly*  
752 *Journal of the Royal Meteorological Society*, **130** (604), 3055–3079, <https://doi.org/10.1256/qj.03.130>.
- 754 Derin, Y., and Coauthors, 2019: Evaluation of GPM-era global satellite precipitation products over  
755 multiple complex terrain regions. *Remote Sensing*, **11** (24).

- 756 Emanuel, K. A., J. David Neelin, and C. S. Bretherton, 1994: On large-scale circulations in  
757 convecting atmospheres. *Quarterly Journal of the Royal Meteorological Society*, **120** (519),  
758 1111–1143, <https://doi.org/10.1002/qj.49712051902>.
- 759 Espinoza, J. C., S. Chavez, J. Ronchail, C. Junquas, K. Takahashi, and W. Lavado, 2015: Rainfall  
760 hotspots over the southern tropical andes: Spatial distribution, rainfall intensity, and rela-  
761 tions with large-scale atmospheric circulation. *Water Resources Research*, **51** (5), 3459–3475,  
762 <https://doi.org/10.1002/2014WR016273>.
- 763 Grossman, R. G., and D. R. Durran, 1984: Interaction of low-level flow with the western ghat  
764 mountains and offshore convection in the summer monsoon. *Monthly Weather Review*, **112**,  
765 652–672, [https://doi.org/10.1175/1520-0493\(1984\)112<0652:IOLLFW>2.0.CO;2](https://doi.org/10.1175/1520-0493(1984)112<0652:IOLLFW>2.0.CO;2).
- 766 Hersbach, H., and Coauthors, 2018: ERA5 hourly data on pressure levels from 1959 to present.  
767 Copernicus Climate Change Service (C3S) Climate Data Store (CDS), accessed: 2021-09-24,  
768 <https://doi.org/10.24381/cds.bd0915c6>.
- 769 Hersbach, H., and Coauthors, 2020: The ERA5 global reanalysis. *Quarterly Journal of the Royal  
770 Meteorological Society*, **146** (730), 1999–2049, <https://doi.org/10.1002/qj.3803>.
- 771 Houze, R. A., 2012: Orographic effects on precipitating clouds. *Reviews of Geophysics*, **50** (1),  
772 <https://doi.org/10.1029/2011RG000365>.
- 773 Houze, R. A., K. L. Rasmussen, M. D. Zuluaga, and S. R. Brodzik, 2015: The variable nature  
774 of convection in the tropics and subtropics: A legacy of 16 years of the Tropical Rainfall  
775 Measuring Mission satellite. *Reviews of Geophysics*, **53** (3), 994–1021, <https://doi.org/10.1002/2015RG000488>.
- 777 Huffman, G. J., E. T. Stocker, D. T. Bolvin, E. J. Nelkin, and J. Tan, 2019: GPM IMERG Final  
778 Precipitation L3 1 day 0.1 degree x 0.1 degree V06. Edited by Andrey Savtchenko, Greenbelt,  
779 MD, Goddard Earth Sciences Data and Information Services Center (GES DISC), accessed:  
780 2021-11-11, <https://doi.org/10.5067/GPM/IMERGDF/DAY/06>.
- 781 Hunt, K. M. R., A. G. Turner, T. H. M. Stein, J. K. Fletcher, and R. K. H. Schiemann, 2021: Modes  
782 of coastal precipitation over southwest india and their relationship with intraseasonal variability.

- 783      *Quarterly Journal of the Royal Meteorological Society*, **147** (734), 181–201, <https://doi.org/10.1002/qj.3913>.
- 784
- 785      Iguchi, T., and R. Meneghini, 2021: GPM DPR Precipitation Profile L2A 1.5 hours 5 km V07.  
786      Greenbelt, MD, Goddard Earth Sciences Data and Information Services Center (GES DISC),  
787      accessed: 2022-11-21, <https://doi.org/10.5067/GPM/DPR/GPM/2A/07>.
- 788      Johnston, B. R., W. J. Randel, and J. P. Sjoberg, 2021: Evaluation of tropospheric moisture  
789      characteristics among COSMIC-2, ERA5 and MERRA-2 in the tropics and subtropics. *Remote*  
790      *Sensing*, **13** (5), <https://doi.org/10.3390/rs13050880>.
- 791      Kirshbaum, D. J., B. Adler, N. Kalthoff, C. Barthlott, and S. Serafin, 2018: Moist orographic  
792      convection: Physical mechanisms and links to surface-exchange processes. *Atmosphere*, **9** (3),  
793      <https://doi.org/10.3390/atmos9030080>.
- 794      Kirshbaum, D. J., and R. B. Smith, 2008: Temperature and moist-stability effects on midlatitude  
795      orographic precipitation. *Quarterly Journal of the Royal Meteorological Society*, **134** (634),  
796      1183–1199, <https://doi.org/10.1002/qj.274>.
- 797      Kumar, S., and G. S. Bhat, 2017: Vertical structure of orographic precipitating clouds observed  
798      over south asia during summer monsoon season. *Journal of Earth System Science*, **126** (8), 114,  
799      <https://doi.org/10.1007/s12040-017-0897-9>.
- 800      Li, D., and Coauthors, 2022: High mountain Asia hydropower systems threatened by climate-  
801      driven landscape instability. *Nature Geoscience*, **15** (7), 520–530, <https://doi.org/10.1038/s41561-022-00953-y>.
- 802
- 803      Lindzen, R. S., and S. Nigam, 1987: On the role of sea surface temperature gradients in forcing  
804      low-level winds and convergence in the tropics. *Journal of Atmospheric Sciences*, **44** (17), 2418  
805      – 2436, [https://doi.org/10.1175/1520-0469\(1987\)044<2418:OTROSS>2.0.CO;2](https://doi.org/10.1175/1520-0469(1987)044<2418:OTROSS>2.0.CO;2).
- 806      Lyon, B., H. Cristi, E. R. Verceles, F. D. Hilario, and R. Abastillas, 2006: Seasonal reversal of the  
807      ENSO rainfall signal in the philippines. *Geophysical Research Letters*, **33** (24), <https://doi.org/10.1029/2006GL028182>.
- 808
- 809      National Geophysical Data Center, 2011: Etopo1, global 1 arc-minute ocean depth and land  
810      elevation from the us national geophysical data center (ngdc). Research Data Archive at the

- 811 National Center for Atmospheric Research, Computational and Information Systems Laboratory,  
812 Boulder CO, accessed 10 Sep 2022, <https://doi.org/10.5065/D69Z92Z5>.
- 813 Nicolas, Q., and W. R. Boos, 2022: A theory for the response of tropical moist convection to  
814 mechanical orographic forcing. *Journal of the Atmospheric Sciences*, **79** (7), 1761 – 1779,  
815 <https://doi.org/10.1175/JAS-D-21-0218.1>.
- 816 Nugent, A. D., R. B. Smith, and J. R. Minder, 2014: Wind speed control of tropical orographic  
817 convection. *Journal of the Atmospheric Sciences*, **71** (7), 2695 – 2712, <https://doi.org/10.1175/JAS-D-13-0399.1>.
- 819 Ogura, Y., and M. Yoshizaki, 1988: Numerical study of orographic-convective precipitation over  
820 the eastern arabian sea and the ghat mountains during the summer monsoon. *Journal of At-  
821 mospheric Sciences*, **45** (15), 2097 – 2122, [https://doi.org/10.1175/1520-0469\(1988\)045<2097: NSOOCP>2.0.CO;2](https://doi.org/10.1175/1520-0469(1988)045<2097: NSOOCP>2.0.CO;2).
- 823 Oouchi, K., A. T. Noda, M. Satoh, B. Wang, S.-P. Xie, H. G. Takahashi, and T. Yasunari,  
824 2009: Asian summer monsoon simulated by a global cloud-system-resolving model: Diurnal  
825 to intra-seasonal variability. *Geophysical Research Letters*, **36** (11), <https://doi.org/10.1029/2009GL038271>.
- 827 Pradhan, R. K., and Coauthors, 2022: Review of GPM IMERG performance: A global perspective.  
828 *Remote Sensing of Environment*, **268**, 112 754, <https://doi.org/10.1016/j.rse.2021.112754>.
- 829 Queney, P., 1948: The problem of air flow over mountains: A summary of theoretical  
830 studies. *Bulletin of the American Meteorological Society*, **29** (1), 16 – 26, <https://doi.org/10.1175/1520-0477-29.1.16>.
- 832 Ramesh, N., Q. Nicolas, and W. R. Boos, 2021: The globally coherent pattern of au-  
833 tumn monsoon precipitation. *Journal of Climate*, **34** (14), 5687 – 5705, <https://doi.org/10.1175/JCLI-D-20-0740.1>.
- 835 Raymond, D., Ž. Fuchs, S. Gjorgjievska, and S. Sessions, 2015: Balanced dynamics and convection  
836 in the tropical troposphere. *Journal of Advances in Modeling Earth Systems*, **7** (3), 1093–1116,  
837 <https://doi.org/10.1002/2015MS000467>.

- 838 Raymond, D. J., S. L. Sessions, A. H. Sobel, and Ž. Fuchs, 2009: The mechanics of gross moist  
839 stability. *Journal of Advances in Modeling Earth Systems*, **1** (3).
- 840 Revadekar, J., H. Varikoden, P. Murumkar, and S. Ahmed, 2018: Latitudinal variation in  
841 summer monsoon rainfall over Western Ghat of India and its association with global sea  
842 surface temperatures. *Science of The Total Environment*, **613-614**, 88–97, <https://doi.org/https://doi.org/10.1016/j.scitotenv.2017.08.285>.
- 844 Robe, F. R., and K. A. Emanuel, 2001: The effect of vertical wind shear on radiative–convective  
845 equilibrium states. *Journal of the Atmospheric Sciences*, **58** (11), 1427 – 1445, [https://doi.org/10.1175/1520-0469\(2001\)058<1427:TEOVWS>2.0.CO;2](https://doi.org/10.1175/1520-0469(2001)058<1427:TEOVWS>2.0.CO;2).
- 847 Robertson, A. W., V. Moron, J.-H. Qian, C.-P. Chang, F. Tangang, E. Aldrian, T. Y. Koh, and  
848 J. Liew, 2011: The maritime continent monsoon. *The Global Monsoon System: Research and*  
849 *Forecast*, 2nd ed., World Scientific, 85–98, [https://doi.org/10.1142/9789814343411\\_0006](https://doi.org/10.1142/9789814343411_0006).
- 850 Roe, G. H., 2005: Orographic precipitation. *Annual Review of Earth and Planetary Sciences*,  
851 **33** (1), 645–671, <https://doi.org/10.1146/annurev.earth.33.092203.122541>.
- 852 Sawyer, J. S., 1956: The physical and dynamical problems of orographic rain. *Weather*, **11** (12),  
853 375–381, <https://doi.org/10.1002/j.1477-8696.1956.tb00264.x>.
- 854 Shige, S., Y. Nakano, and M. K. Yamamoto, 2017: Role of orography, diurnal cycle, and intrasea-  
855 sonal oscillation in summer monsoon rainfall over the western ghats and myanmar coast. *Journal*  
856 *of Climate*, **30** (23), 9365 – 9381, <https://doi.org/10.1175/JCLI-D-16-0858.1>.
- 857 Shrestha, D., R. Deshar, and K. Nakamura, 2015: Characteristics of summer precipitation around  
858 the western ghats and the myanmar west coast. *International Journal of Atmospheric Sciences*,  
859 **2015**, 206 016, <https://doi.org/10.1155/2015/206016>.
- 860 Sijikumar, S., L. John, and K. Manjusha, 2013: Sensitivity study on the role of western ghats in  
861 simulating the asian summer monsoon characteristics. *Meteorology and Atmospheric Physics*,  
862 **120** (1), 53–60, <https://doi.org/10.1007/s00703-013-0238-8>.
- 863 Sikka, D. R., 1977: Some aspects of the life history, structure and movement of monsoon depres-  
864 sions. *Pure and Applied Geophysics*, **115** (5), 1501–1529, <https://doi.org/10.1007/BF00874421>.

- 865 Smith, I., A. Moise, K. Inape, B. Murphy, R. Colman, S. Power, and C. Chung, 2013: Enso-related  
866 rainfall changes over the new guinea region. *Journal of Geophysical Research: Atmospheres*,  
867 **118 (19)**, 10,665–10,675, <https://doi.org/10.1002/jgrd.50818>.
- 888 Smith, R. B., 1979: The influence of mountains on the atmosphere. *Advances in Geophysics*, **21**,  
869 87–230, [https://doi.org/10.1016/S0065-2687\(08\)60262-9](https://doi.org/10.1016/S0065-2687(08)60262-9).
- 870 Smith, R. B., 1989: Hydrostatic airflow over mountains. *Advances in Geophysics*, **31**, 1–41.
- 871 Smith, R. B., 2018: 100 Years of Progress on Mountain Meteorology Research. *Meteorological Monographs*, Vol. 59, American Meteorological Society, 20, <https://doi.org/10.1175/AMSMONOGRAPHSD-18-0022.1>.
- 874 Smith, R. B., and I. Barstad, 2004: A linear theory of orographic precipitation. *Journal of the Atmospheric Sciences*, **61 (12)**, 1377 – 1391, [https://doi.org/10.1175/1520-0469\(2004\)061<1377:ALTOOP>2.0.CO;2](https://doi.org/10.1175/1520-0469(2004)061<1377:ALTOOP>2.0.CO;2).
- 875 Smith, R. B., and Y.-L. Lin, 1983: Orographic rain on the western ghats. *Proceedings of the First  
876 Sino-American Workshop on Mountain Meteorology*, 71–94.
- 879 Sobel, A. H., C. D. Burleyson, and S. E. Yuter, 2011: Rain on small tropical islands. *Journal of  
880 Geophysical Research: Atmospheres*, **116 (D8)**, <https://doi.org/10.1029/2010JD014695>.
- 881 Sobel, A. H., J. Nilsson, and L. M. Polvani, 2001: The weak temperature gradient approximation  
882 and balanced tropical moisture waves. *Journal of the Atmospheric Sciences*, **58 (23)**, 3650 –  
883 3665, [https://doi.org/10.1175/1520-0469\(2001\)058<3650:TWTGAA>2.0.CO;2](https://doi.org/10.1175/1520-0469(2001)058<3650:TWTGAA>2.0.CO;2).
- 884 Tawde, S. A., and C. Singh, 2015: Investigation of orographic features influencing spatial distribution  
885 of rainfall over the western ghats of india using satellite data. *International Journal of  
886 Climatology*, **35 (9)**, 2280–2293, <https://doi.org/10.1002/joc.4146>.
- 887 Van den Hende, C., B. Van Schaeybroeck, J. Nyssen, S. Van Vooren, M. Van Ginderachter,  
888 and P. Termonia, 2021: Analysis of rain-shadows in the Ethiopian mountains using  
889 climatological model data. *Climate Dynamics*, **56 (5)**, 1663–1679, <https://doi.org/10.1007/s00382-020-05554-2>.

- 891 Vivioli, D., M. Kummu, M. Meybeck, M. Kallio, and Y. Wada, 2020: Increasing dependence  
892 of lowland populations on mountain water resources. *Nature Sustainability*, **3** (11), 917–928,  
893 <https://doi.org/10.1038/s41893-020-0559-9>.
- 894 Wang, S., and A. H. Sobel, 2017: Factors controlling rain on small tropical islands: Diurnal  
895 cycle, large-scale wind speed, and topography. *Journal of the Atmospheric Sciences*, **74** (11),  
896 3515–3532.
- 897 Wilks, D. S., 2016: “the stippling shows statistically significant grid points”: How research results  
898 are routinely overstated and overinterpreted, and what to do about it. *Bulletin of the American  
899 Meteorological Society*, **97** (12), 2263 – 2273, <https://doi.org/10.1175/BAMS-D-15-00267.1>.
- 900 Wu, C.-H., W.-R. Huang, and S.-Y. S. Wang, 2018: Role of indochina peninsula topography in pre-  
901 cipitation seasonality over east asia. *Atmosphere*, **9** (7), <https://doi.org/10.3390/atmos9070255>.
- 902 Xie, S.-P., H. Xu, N. H. Saji, Y. Wang, and W. T. Liu, 2006: Role of narrow mountains in large-  
903 scale organization of asian monsoon convection. *Journal of Climate*, **19** (14), 3420 – 3429,  
904 <https://doi.org/10.1175/JCLI3777.1>.
- 905 Yen, M.-C., T.-C. Chen, H.-L. Hu, R.-Y. Tzeng, D. T. Dinh, T. T. T. Nguyen, and C. J. Wong,  
906 2011: Interannual variation of the fall rainfall in central Vietnam. *Journal of the Meteorological  
907 Society of Japan. Ser. II*, **89A**, 259–270, <https://doi.org/10.2151/jmsj.2011-A16>.
- 908 Zhang, G., and R. B. Smith, 2018: Numerical study of physical processes controlling sum-  
909 mer precipitation over the Western Ghats region. *Journal of Climate*, **31** (8), 3099 – 3115,  
910 <https://doi.org/10.1175/JCLI-D-17-0002.1>.